

Decadal variations in the Southern Ocean carbon sink in MPI-ESM 100 ensemble simulations

Aaron Spring

May 29, 2017

Outline

Contents

1	Introduction	3
2	Methods	5
2.1	Model description of the MPI-ESM	5
2.2	Large ensemble simulations	10
2.3	Observational data	11
2.4	Statistical methods	12
2.5	Climatological methods	13
3	Model evaluation of the Southern Ocean	15
3.1	CO ₂ flux	15
3.2	Winds	19
3.3	Biology	22
3.4	Upper-Ocean Overturning Circulation	26
4	Trends in CO₂ flux	29
4.1	Winds determine internal variability of the Southern Ocean CO ₂ flux	29
4.2	Positive CO ₂ flux trends	31
4.3	Negative CO ₂ flux trends	38
5	Distinction of drivers in pCO₂	44
5.1	Derivation of the framework	44
5.2	Estimate of pCO ₂ drivers	47
6	Summary and conclusions	51
A	Supplementary information	72

1 Introduction

Why the Southern Ocean is important The oceans are major carbon sink by taking up about 25-30% of the anthropogenic carbon emissions from the atmosphere [Le Quéré et al., 2016]. As a key region, the Southern Ocean contributes about 40% to the global ocean carbon sink [Sabine et al., 2004]. Due to the sparse spatial and temporal coverage in the Southern Ocean, various observational CO₂ flux products yield large uncertainties [Rödenbeck et al., 2015]. Also modeling results have a large spread [Wang et al., 2016], but claim the Southern Ocean as a constraint to reduce model uncertainties [Kessler and Tjiputra, 2016].

Southern Ocean observations and demand for models Recent observations suggest pronounced decadal variations in the Southern Ocean carbon sink [Rödenbeck et al., 2013, Landschützer et al., 2015]. However, due to the sparse spatial and temporal coverage, it is challenging to discern the dynamics of internally varying processes, which demands for the evaluation with models. Earth system models (ESMs) are a useful tool to analyze processes that contribute to variability. Lovenduski et al. [2007, 2008] explained the mechanistic processes behind the positive trend in the Southern Annular Mode with a ocean model with atmospheric forcing from reanalysis data. Yet, ESMs, containing a freely evolving coupled atmospheric and ocean component, don't capture the decadal variations suggest by observations [Wang et al., 2016]. Using a large ensemble of simulations with perturbed initial conditions but identical forcing and model allows to separate the forced signal and internal variability.

What I do and research questions By using a large ensemble simulation based on the Max-Planck-Institute Earth System Model (MPI-ESM), I investigate the variability of the oceanic carbon uptake. I try to answer the following research questions:

- What is the modeled internal variability of the Southern Ocean carbon sink?
- How does variability in biological and physical processes influence the carbon sink?

Working hypothesis The Southern Annular Mode (SAM), characterizing the strength and position of the westerly winds, is known to be the dominant mode of climate variability in the Southern hemisphere [Thompson and Wallace, 2000, Thompson et al., 2011]. Supposing the strength and position of the westerlies winds as the major reason for climate variability for the Southern Ocean [Thompson and Wallace, 2000], how does the carbon system respond? Changes in westerly winds alter circulation patterns, which directly effect the carbon sink via the thermal effect, circulation of carbon and biological production.

Revisit processes In this thesis, I revisit the dominant processes leading to extreme trends in the Southern Ocean carbon sink in the biogeochemical model HAMOCC [similar Lovenduski et al. [2007, 2008], as individual processes related to changes in winds are already discussed for changes in temperature [Takahashi et al., 1993, Lovenduski et al., 2007], circulation [Abernathay et al., 2011, Hauck et al., 2013, Lauderdale et al., 2016, Lovenduski et al., 2008] and biology [Lovenduski and Gruber, 2005, Tagliabue et al., 2014, Wang and Moore, 2012]. This revisit is particularly interesting as other large ensembles of perturbed initial conditions do not capture strong decadal variations in the Southern Ocean carbon sink whereas MPI-ESM LE does [private communication N. Lovenduski (NCAR) and S. Schlunegger (GFDL), see section 2.2 for details].

2 Methods

2.1 Model description of the MPI-ESM

The Max-Planck-Institute for Meteorology Earth System Model (MPI-ESM) consists of coupled general circulation models of the atmosphere ECHAM6 [Stevens et al., 2013] and ocean MPIOM [Jungclaus et al., 2013] as well as subsystem models for vegetation on land JSBACH [Reick et al., 2013] and for marine biogeochemistry HAMOCC [Ilyina et al., 2013]. The large ensemble simulations are based on MPI-ESM version 1.1.00p2¹ with a low-resolution configuration. Since the atmospheric pCO₂ levels are prescribed, terrestrial carbon cycle from the land component JSBACH and oceanic carbon cycle from HAMOCC do not interact (fig. 1). The full earth-system model [Giorgetta et al., 2013] as well as its components have been described and evaluated in detail by the given references. In the following subsections, I give an overview about the implemented processes affecting internal variability of the oceanic carbon cycle.

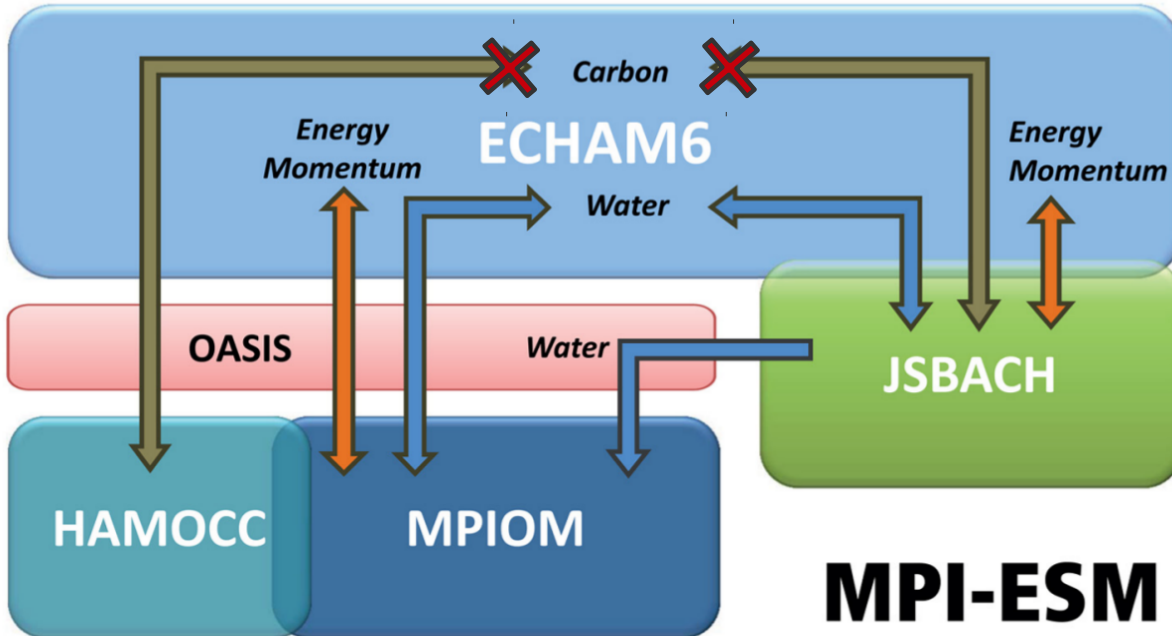


Figure 1: Schematic overview on the different components in MPI-Earth-System-Model with a non-interactive carbon cycle [Giorgetta et al., 2013]

¹full source code: <https://code.zmaw.de/projects/mpi-esm/repository/show/tags/mpiesm-1.1.00p2>

2.1.1 ECHAM

ECHAM - a naming combination of European Center (EC) for Medium Range Weather Forecasts (ECMWF) and HAM for Hamburg - is an general circulation model for the atmosphere. ECHAM has an air-sea gas exchange interface with HAMOCC and exchanges water, energy and momentum with MPIOM. The atmosphere component ECHAM6.3 runs on a T63 grid, corresponding to 1.9° horizontal resolution, with 47 vertical layers up to 0.01 hPa [Stevens et al., 2013]. This high vertical resolution and atmospheric height allows to model jets which originate in the tropopause. Those jets define the position and strength of the westerly winds in the Southern hemisphere. In ECHAM extratropical jets are slightly shifted to lower latitudes [Stevens et al., 2013] which seems to be a common atmospheric modeling challenge [Kidston and Gerber, 2010]. Changes in ECHAM with regard to CMIP5 version in Stevens et al. [2013] are described in Bittner et al. [2016]. They majorly include a new radiation code of ECHAM6.3 which leads to small changes in the temperature fields.

2.1.2 MPIOM

The ocean model MPIOM is an ocean general circulation model (OGCM) with a horizontal resolution of 1.5° on average on the Arakawa C-grid, 40 fixed-depth vertical levels on a realistic topography and with a free surface [Jungclaus et al., 2013]. All biogeochemical and physical tracers except for opal and calcite shells are advected by the Navier-Stokes equations with Boussinesq-approximation [Marsland et al., 2003]. In areas of large scale upwelling - such as the Southern Ocean - those tracers are advected to the ocean surface. Those carbon-rich waters then equilibrate with atmospheric pCO_2 . Upwelling processes are largely driven by divergence due to winds. Strong ocean currents lead to eddies which additionally mix the water column horizontally and vertically. The spatial resolution of 1.5° translated to a grid cell length of ~ 150 km at the northern edge of the Southern Ocean at 30°S and ~ 40 km in Antarctic coastal waters. These length scales are too small to resolve eddies, so they are parametrized by the GM-scheme [Gent et al., 1995]. Therefore, the vertical mixing and diffusion based on Richardson-number dependent formulation is important for vertical gradients [Pacanowski and Philander, 1981]. The impact of eddies on the carbon cycle, especially in the Southern Ocean, is under current research [Lauderdale et al., 2013, Dufour et al., 2013, Gnanadesikan et al., 2015].

The mixed-layer depth is calculated by a potential density criterion where the difference between the sea-surface density and the lower end of the mixed-layer is 0.125 kg m^{-3} [Jungclaus et al., 2013].

2.1.3 HAMOCC

The Hamburg Ocean Carbon Cycle model HAMOCC is a global marine carbon cycle model which simulates oceanic carbon and nutrient cycles [Maier-Reimer, 1984, 1993, Six and Maier-Reimer, 1996]. It aims to reproduce distributions of biogeochemical parameters over various timescales from seasons to millenia without regional tuning or temporal adjustments towards observations. This includes processes on three compartments: air-sea interactive at the sea surface, biogeochemistry of the water column and sediment biogeochemistry (fig. 2). The HAMOCC model version for the large ensemble is identical to the one used in CMIP5 which is analyzed in detail in Ilyina et al. [2013]. In the following subsection, I can only give an overview about the most relevant processes for the variability on decadal and shorter timescales.

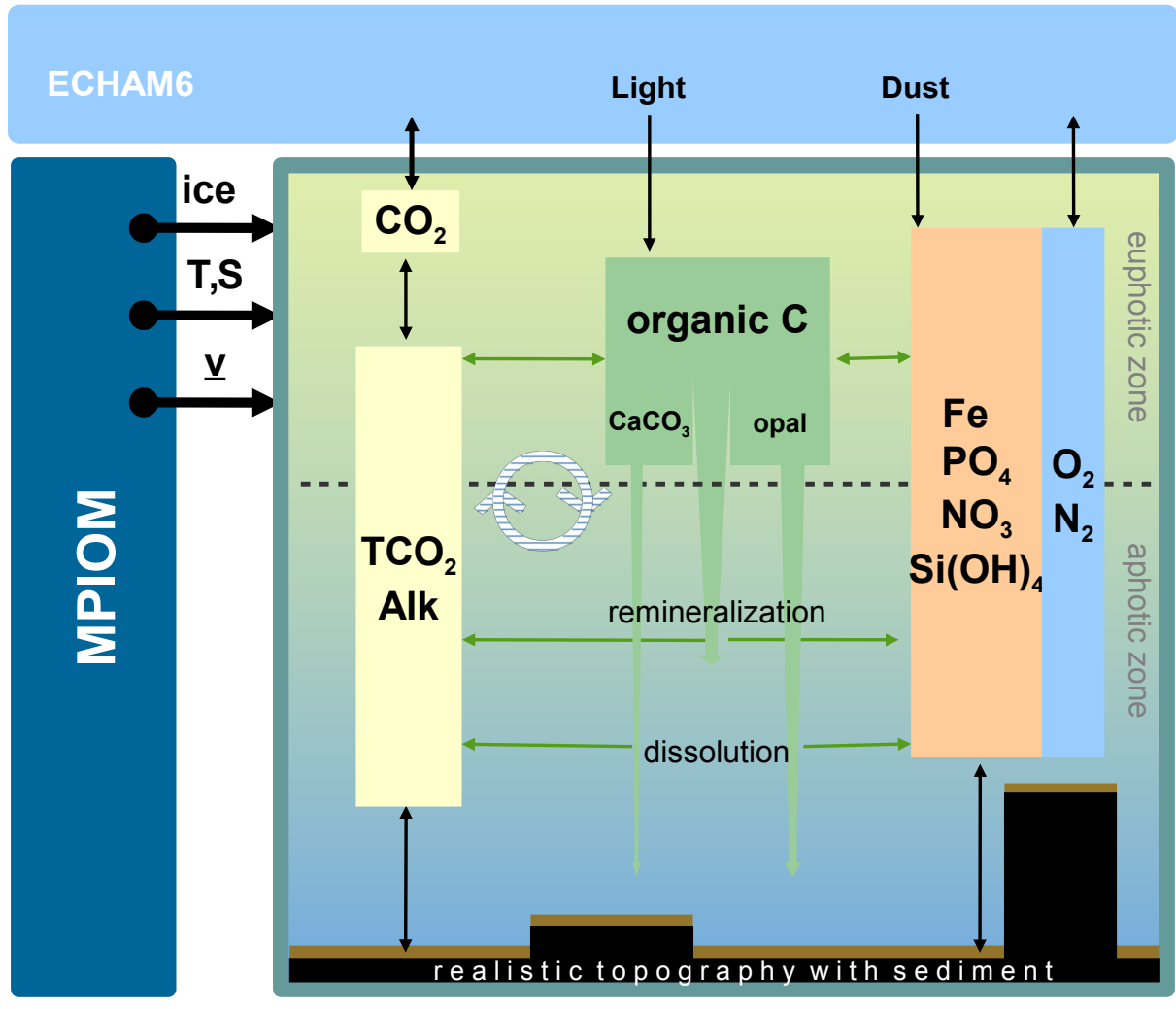
CO₂ flux description The CO₂ flux calculation implemented in the model follows an empirical relationship under the conceptual one-layer ocean-sided stagnant film model with gas transfer velocity k_w [Wanninkhof, 1992]:

$$\begin{aligned} \text{CO}_2\text{flux} &= (1 - f)k_w\Delta p\text{CO}_2 \\ k_w &= 0.31u_{10}^2(\text{Sc}(T)/660)^{-1/2} \\ \Delta p\text{CO}_2 &= p\text{CO}_{2,\text{ocean}} - p\text{CO}_{2,\text{atm}}, \end{aligned}$$

where f is the sea-ice fraction of the grid cell, u_{10} is the wind speed at 10 m height, Sc is the temperature-dependent Schmidt number, 660 is the Schmidt number of CO₂ in seawater at 20°C, and $\Delta p\text{CO}_2$ is the difference between the partial pressure of CO₂ in the atmosphere and the ocean, so positive values of CO₂ flux represent a net flux from the ocean to the atmosphere. The potential partial pressure of CO₂ in water $p\text{CO}_{2,\text{ocean}}$ is solubility-dependent by Henry's law and calculated according to [Weiss, 1974]. The solubility is primarily temperature sensitive. Ocean warming decreases solubility, whereas cooling increases it. Therefore saturated surface waters outgas when heated - a process referred to as the solubility pump of carbon [Volk and Hoffert, 1985].

CO₂ flux variability The disequilibrium $\Delta p\text{CO}_2$ drives CO₂ flux variability by setting the direction of CO₂ flux. As $p\text{CO}_{2,\text{atm}}$ is prescribed in the MPI-ESM LE, changes in $p\text{CO}_{2,\text{ocean}}$ are the main driver of CO₂ flux variability. The carbonate chemistry directly relates $p\text{CO}_{2,\text{ocean}}$ to surface dissolved inorganic carbon (DIC). Besides CO₂ flux, surface DIC is mainly changed by biology (see below) and advection (see section 2.1.2).

Biology In the euphotic zone up to a depth of 90m, phytoplankton converts inorganic nutrients, e.g. phosphate (PO₄), nitrate (NO₃), and iron, and inorganic carbon to organic matter by photosynthesis. The predator-prey relationship in HAMOCC follows a



HAMOCC

Figure 2: Schematic overview of the global ocean biogeochemistry model HAMOCC [Ilyina et al., 2013] which is coupled to the atmospheric model component ECHAM and the ocean model MPIOM. The ocean model provides state variables of physical oceanography, i.e. ice cover, temperature (T), salinity (S) and the advective velocities (\bar{v}). The water column holds tracers of gases, i.e. oxygen (O_2), nitrogen (N_2), laughing gas (N_2O), and dimethyl sulfide (DMS); nutrients, i.e. iron (Fe), phosphate (PO_4), nitrate (NO_3) and silicic acid $\text{Si}(\text{OH})_4$; and tracers of carbonate chemistry, i.e. dissolved inorganic carbon (TCO_2) and total alkalinity (TA). Photosynthesis converts DIC and nutrients to organic carbon, which produces calcium carbon (CaCO_3) or opal shells.

NPZD model [Six and Maier-Reimer, 1996]. Phytoplankton proliferate from nutrient consumption. Zooplankton consume phytoplankton, while detritus forms as opal and calcium carbonate shells and sinks down the water column, a process referred to as the biological pump [Volk and Hoffert, 1985]. While detritus sinks to the ocean floor, it partly remineralizes and gives rise to nutrient and DIC concentrations, which can lead to outgassing once they are advected to the surface.

Phytoplankton growth is co-limited by nutrients (phosphate, nitrate and iron), temperature and light: Phytoplankton is parametrized by bulk phytoplankton, which mimics the combined growth of diatoms, coccolithophores and dinoflagellates under exponentially increasing optimum growth rate temperatures [Eppley, 1972]. Phytoplankton growth depends linearly on the availability of light, without saturation for stronger irradiance. Platt and Jassby [1976] found a good fit to observations by the limiting function of Smith [1936] describing the limiting behavior of light and temperature [Six and Maier-Reimer, 1996] (see fig. A.13). Michaelis-Menten kinetics describe the nutrient limitation of the maximum phytoplankton growth rate with a half-saturation constant [Michaelis and Menten, 1913]. The limiting role of nutrients is described by the nutrient availability factor that multiplies with the average growth rate of phytoplankton. The macro-nutrient iron is modeled explicitly. It enters the water column via a monthly dust input climatology, is used in photosynthesis and released in remineralization.

Variability in biology due to changing physical conditions Biological processes are strongly dependent on physical properties of the ocean circulation. Mixing can change the nutrient distributions, when remineralized nutrients from the deep ocean mix into the eutrophic zone. Mixing can also pull the standing stock of phytoplankton deeper into the ocean where less light is available which inhibits growth. Changes in sea surface temperature also directly affect phytoplankton growth.

Also the atmosphere alters biological production: Cloud-cover reduces photosynthetic active radiation and freshwater fluxes can dilute nutrient concentrations.

Misc with low impact on carbon variability: chemistry and sediment Other processes in a biogeochemical model act on longer timescales or small amplitude and hence lack a strong variability signal in the carbon cycle.

The chemistry in HAMOCC models the carbonate system and keeps track of alkalinity [Maier-Reimer, 1993]. Dissolved inorganic carbon and alkalinity are directly calculated as prognostic tracers from which other tracers derived.

For falling detritus, there exist two different parts: opal producing if silicate is available or calcium carbonate producing. Calcification then changes the alkalinity and carbon budget.

Once detritus reach the the ocean floor, particulate matter enters the sediment and finally the burial layer. At the boundary of the sediment, all tracers are in exchange with the sediment which via pore water exchange [Heinze et al., 1999].

2.2 Large ensemble simulations

Perturbed initial conditions large ensembles Large ensemble simulations are a novel tool to investigate model internal variability. "Climate variability refers to variations in the mean state (...), which may be due to natural internal processes within the climate system (internal variability), or to variations in natural or anthropogenic external forcing (external variability)" [IPCC, 2013]. The variability in observations is impossible to separate, if - like in the case of pCO₂ no long-lasting direct measurement records exist. Although modeled internal variability is not equivalent to observed internal variability, we can learn about the chaotic behavior of natural processes.

By iterating a climate simulation with an identical forcing and model code but slightly perturbed initial conditions, single ensemble members will be exposed to the same process implementations. The interplay of those at stochastically random level lets each realization evolve in a unique way while still being bound to a common forced signal, which follows the external forcing. Perturbed initial conditions large ensemble simulations allow to distinguish a signal into a force signal, which is the average signal across all ensemble members, and the residual, which modulates the signal around the forced signal due to internal variability [Ilyina, 2016]:

$$\text{signal} = \text{forced signal} + \text{internal variability}.$$

MPI-ESM Large Ensemble The MPI-ESM Large Ensemble (MPI-ESM LE) contains 100 simulations under historical CMIP5 forcing from 1850 to 2005 and is extended under Representative Concentration Pathway (RCP) 4.5 scenario until 2100, so the forcing includes volcano eruptions from the historical period and solar cycles. Anthropogenic forcings include well-mixed greenhouse gases, anthropogenic sulphate aerosols and man-made land use change. Atmospheric pCO₂ levels are prescribed according to the CMIP5 protocol [Taylor et al., 2012]. The carbon cycle is not coupled, so effects of changes in the terrestrial or oceanic carbon sink are not reflected in the atmospheric pCO_{2,atm}.

Ensemble members differ through starting from different year of the pre-industrial control simulation, so ocean and atmosphere have slightly different initial conditions in each run. This was achieved by branching off ensemble members from a 2000-year pre-industrial control run after roughly 50 years, when atmospheric pCO₂ levels were increased.

The historical part of MPI-ESM from 1850 to 2005 was calculated at the Swiss National Supercomputing Centre (CSCS), the extension on the supercomputer Mistral at the German climate research center (DKRZ). The model and run script were compatible, however different hardware and compilers might lead to changes in variability distributions. Therefore, I restrict the analysis of decadal internal variability to the timeframe between 1980, the beginning of the observational dataset and 2005.

Other large ensemble simulations As running large ensembles simulation comes with high computational costs, this area of climate modeling research is still more recent.

There are only a few datasets available and published papers are infrequent.

NCAR's Community Earth System Model large ensemble (CESM LE) [Kay et al., 2015] lead to the first studies of perturbed initial conditions large ensembles on internal variability by Deser et al. [2012]. CESM LE served for studies analyzing the timescales of detection of trend in the ocean carbon sink [McKinley et al., 2016] and the partitioning if its uncertainties [Lovenduski et al., 2016].

The initial state of the atmosphere was slightly perturbed by roundoff-level changes to air temperature in their 32 runs.

Although the initialization of ensembles differs, the variability after a few model years is not affected anymore by initialization method, but by model variability [some study].

CESM LE studies like Deser et al. [2012] and Thompson et al. [2015] assume Gaussian statistics. In section 2.4.3, I show that our larger ensemble generates spatial and temporal distributions with statistics similar to gaussian distributions.

GFDL ran a 30-member ensemble simulation based on their model ESM2M. They use different dates separated by one day each but didn't publish any oceanic carbon uptake paper yet [Rodgers et al., 2015].

2.3 Observational data

There are large uncertainties in observational-based CO₂ flux products, especially in the Southern Ocean [Rödenbeck et al., 2015]. Direct pCO₂ measurements in the Southern Ocean are sparse and discontinuous. Different mapping techniques lead to a spread in observation-based estimates.

For comparison of CO₂ flux with model simulations, I use the Self-Organizing Map-Feed-Forward Network (SOM-FFN) data which is based on the Surface Ocean Atlas Version 2 (SOCATv2) [Bakker et al., 2014]. It uses a neural network-based data interpolation to create pCO₂ maps [Landschützer et al., 2014]. The data product is smoothed by a 3x3 filter averaging two months and the neighboring grid cells, but this has little effect on seasonal dynamics as this study focuses on the decadal variability. I use this pCO₂ data product because this method takes multiple variables for pCO₂ interpolation to cover regions without direct pCO₂ measurements. However, the input training data of the algorithm is seasonally biased, as the available pCO₂ samples originate mostly from austral summer months.

However, SOM-FFN as well as the mixed-layer scheme Jena-MLS [Rödenbeck et al., 2013, Rödenbeck et al., 2014] produces a relatively low monthly mismatch globally compared to original SOCAT data [Rödenbeck et al., 2015]. Both those data products agree on the decadal trends in the Southern Ocean. As the different data products cannot be validated or falsified, I use SOM-FFN as the best estimate - still acknowledging the current limitations of pCO₂ data.

2.4 Statistical methods

2.4.1 Linear trends and statistical tests

The main tool for analysis - linear trends - is the computation of a linear regression coefficient via least-squares. With Student's t-test, I check in spatial patterns, whether this trend is significantly different to the null hypothesis (see section 4) [Mood et al., 1974]. To exclude seasonal variability, the climatological seasonality is removed from all monthly data before trend computation.

Mann-Kendall test for monotonic trends The Mann-Kendall test is a statistical tool to assess if there is a monotonic upward or downward trend of the variable of interest over time [Mann, 1945, Kendall, 1975]. This test is applied in section 3.1 to extract trends based on a selection criterion of monotony.

Monotonic upward mean that it consistently increases over time. The Mann-Kendall test is best viewed as an exploratory analysis and is most appropriately used to identify stations where changes are significant or of large magnitude [Hirsch et al., 1982].

The Mann-Kendall statistic S counts magnitude relations of each pair of all available timesteps in a dataset with the sign function:

$$S = \sum \operatorname{sgn} (x_k - x_i).$$

This Mann-Kendall statistic S converts to probabilities for monotonic behavior according to Gilbert [1987].

2.4.2 Choice of trends

To analyze the processes driving decadal internal variability σ_{DIV} (see subsection 2.4.3), I focus on individual ensemble realizations in chapters 3 and 4. Here, I have to make a compromise between signal strength and robustness versus trendlength. The longer a period, the more likely the trend deviates from a monotonic behavior, e.g. after a few years of monotonic increase the trend reverses (see fig. 4). Therefore longer trends show less chance to have a strong signal per trendlength (fig. A.2). Also, longer trends experience a stronger influence of atmospheric forced trend. Furthermore, the underlying mechanisms for CO₂ flux trends in our ensemble simulation seem to be of the same origin regardless of the exact length of the trend period. Therefore, I decided to select 8-year trends in chapter 3 to understand the trending processes in chapter 4, because 8-year trends are still very close to a decadal 10-year trends and still able to show similar magnitude and monotonic behavior as the observation-based estimate. Monotonic behavior is maintained by a Mann-Kendall test above a probability threshold of 0.98 ($S_{\text{threshold}} \leq 16$), which does not require strictly monotonic behavior, but allows few deviations.

2.4.3 Decadal internal variability

Internal variability is present on many timescales. To investigate decadal internal variability, I assess the differences of the annual mean state in a decade. Therefore, I define decadal internal variability σ_{DIV} of any variable X as the standard deviation of the changes in M running multi-year (specifically 8-year) decades in all N ensembles:

$$\sigma_{DIV}(X) = \sqrt{\frac{1}{MN} \sum_{n=\text{ens}}^N \sum_{m=\text{yr}}^M (\chi_{m,n} - \bar{\chi}_{m,n})^2}$$

$$\chi_{m,n} = X_{\text{decade}_{\text{end}},n} - X_{\text{decade}_{\text{start}},n}$$

I use values of the annual values to filter out seasonal variability and set the turn of the year to the end of July to fully capture one austral summer season, which allows in-depth analysis for trends in biology.

Gaussian statistics Previous studies assume Gaussian statistics, but lack an adequate ensemble size to check for in detail [Deser et al., 2012, Thompson et al., 2015]. The large ensemble used for this study includes 100 members. Furthermore, I increases my sample size to calculate trends in running intervals between 1980 and 2004.

The temporal distribution of the spatially integrated sum of the whole Southern Ocean (fig. A.1a) as well as of a single randomly chosen grid cell in the Southern Ocean CO₂ flux (fig. A.1b) follows Gaussian statistics. Assuming this also for other variables allows me to use the standard deviation as a metric and interpret those as probabilities.

2.4.4 Weighted average depth

To visualize vertical distributions of the ocean, i.e. average phytoplankton depth or average depth of vertical diffusivity due to wind, I reduce the information of a three-dimensional field to a map and I take a weighted average $\overline{A_z}$ over all depth levels z_i up to the deepest level L of phytoplankton at 90m:

$$\overline{A_z}(x, y) = \sum_{i=1}^L z_i A(x, y, z_i)$$

2.5 Climatological methods

2.5.1 Southern Annular Mode Index

The Southern Ocean westerly winds are variable in strength and location. To describe this variability the Southern Annular Mode (SAM) index, formerly known as the Antarctic Oscillation Index (AOI), was defined by [Gong and Wang \[1999\]](#). To construct the index,

I remove the climatological seasonal cycle from the maps of sea-level pressure and take a zonal mean of the latitudes 40°S and 65°S, standardize them against the climatological period of 1950-1979 as P^* and take the difference to create the index value:

$$SAM = P_{40^\circ S}^* - P_{65^\circ S}^*$$

2.5.2 Thermal separation

In order to separate the influence of temperature on CO₂ flux, I apply the methodology of [Takahashi et al. \[1993, 2002\]](#). The thermal component pCO_{2,thermal} to account for the effect of changes in sea-surface (temperature SST) on pCO₂. The non-thermal component pCO_{2,non-thermal} accounts for changes in DIC and alkalinity:

$$\begin{aligned} pCO_{2,\text{thermal}} &= \overline{pCO_2} \cdot \exp [0.0423^\circ C^{-1} (T - \bar{T})] \\ pCO_{2,\text{non-thermal}} &= pCO_2 \cdot \exp [0.0423^\circ C^{-1} (\bar{T} - T)] . \end{aligned}$$

The overbar indicates the temporal average.

3 Model evaluation of the Southern Ocean

My analysis of the internal variability of the Southern Ocean carbon sink originates in the evaluation of air-sea CO₂ flux (see section 3.1). As the strength of the CO₂ flux in the Southern Ocean is modulated by the strength of westerly winds [Lovenduski et al., 2007], I assess also the sea-level pressure field and winds (see section 3.2), followed by its impact on biology (see section 3.3) and upper-ocean circulation (see section 3.4).

A previous model evaluation of HAMOCC for the Coupled Model Intercomparison Project (CMIP) 5 provides a global view on biogeochemistry [Ilyina et al., 2013]. Here I evaluate the model focusing on the Southern Ocean and specifically the processes related to the carbon sink. In each subsection I compare the modeled mean state of the Southern Ocean to observational data and assess modeled decadal internal variability in spatial distribution and temporal evolution.

3.1 CO₂ flux

The patterns of CO₂ flux are mainly controlled by CO₂-consuming primary production (see in detail section 3.3) and vertical water transport (see in detail section 3.4), where Ekman suction, also referred to as upwelling, drives degassing and Ekman subduction, also referred to as downwelling, CO₂ favors uptake. Positive values indicate degassing and negative values CO₂ uptake by the oceans.

Spatial distribution in mean state The climatological ensemble mean state from 1980 to 2004 of the Southern Ocean CO₂ flux in MPI-ESM marks the Antarctic coastal region as a CO₂ sink, whereas the upwelling waters at 50–60°S are outgassing regions in the Atlantic and Indian sector and CO₂ flux neutral in the Pacific (fig. 3a). North of the subantarctic front (~50°S), the oceans take up CO₂ because of stronger primary production and Ekman subduction.

Spatial mean comparison to observational data SOM-FFN observational-based estimate data show similar patterns of carbon uptake and outgassing, but in lower absolute values (fig. 3c). Hardly any measurements in the region of seasonal ice cover make a comparison with observation-based values hard to interpret.

Spatial distribution of internal variability For spatial distributions, I define decadal internal variability σ_{DIV} as the standard deviation over the changes in decades in the whole ensemble as shown in section 2.4.3.

The region 45–60°S is most variable. This is the area of Ekman suction (compare fig. 10) and the southern edge of primary production area (compare fig. 7). The change in latitudinal position and strength of the westerly winds affects the position and amplitude of upwelling (see section 3.4) and primary production (see section 3.3).

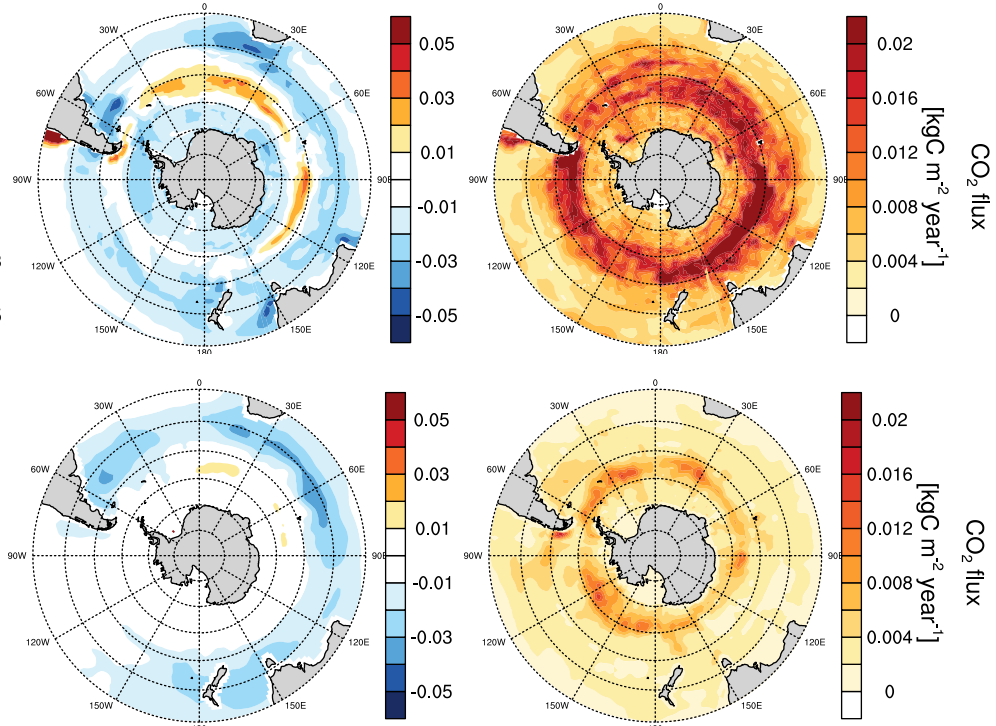


Figure 3: Spatial distribution of the climatology (a,c) and decadal internal variability σ_{DIV} (b,d) from 1980-2004 of the Southern Ocean air-sea CO₂ flux: MPI-ESM LE ensemble mean as forced signal (a), ensemble decadal standard deviation as decadal internal variability σ_{DIV} (b), SOM-FFN climatology 1982-2004 (c), SOM-FFN decadal variability σ_{DIV} (d); negative values indicate ocean uptake.

Spatial variability comparison to observational data The observation-based SOM-FFN decadal variability σ_{DIV} is most pronounced at 50-60°S in the Atlantic and Indian and south of 60°S in the Pacific. The amplitude of decadal variability is smaller than in MPI-ESM (fig. 3d). However, this comparison is limited by large differences in sample size between the 22-year observational record and the 100 MPI-ESM realizations. Reference to CMIP5 mean and std [later in appendix]?

Temporal evolution of the mean state and internal variability The modeled temporal evolution of the Southern Ocean ensemble mean CO₂ flux south of 35°S is dominated by the forced negative trend of rising atmospheric CO₂ concentrations (fig. 4). However, no individual realization follows the negative trend strictly monotonic - they oscillate around the ensemble mean state triggered by internal variability. Exemplary, the most extreme monotonic positive and negative 8-year trend is highlighted. Modeled decadal internal variability σ_{DIV} is 0.22 PgC.

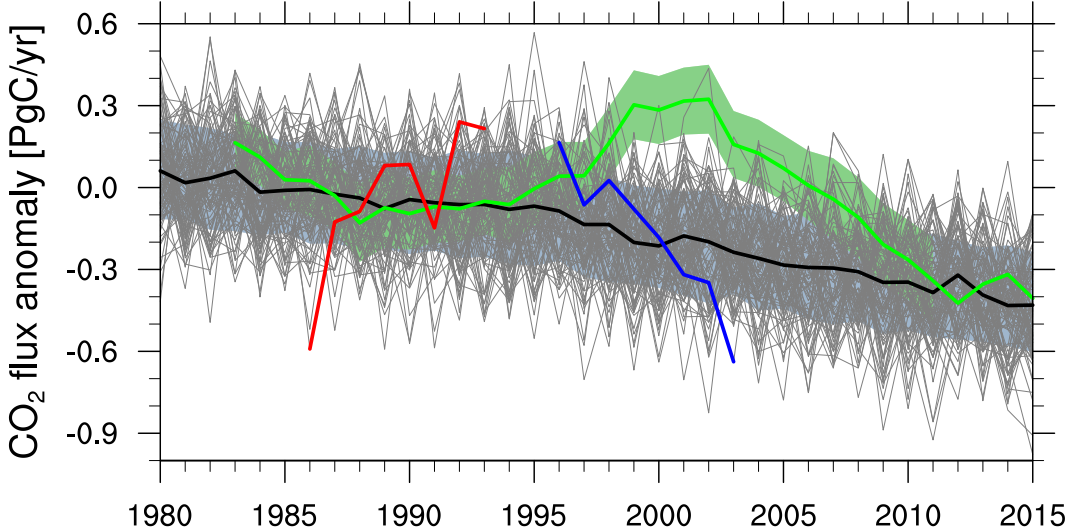


Figure 4: Temporal evolution of the Southern Ocean air-sea CO_2 flux south of 35°S . Grey lines show the 100 ensemble members, the black line the ensemble mean, the blue shading is the ensemble decadal internal variability σ_{DIV} , the red line shows a positive CO_2 flux trend, the blue line shows a negative CO_2 flux trend, the green line represents the SOM-FFN observation-based estimate [Landschützer et al., 2015]; negative values indicate carbon uptake

Temporal comparison to observational data The observational-based estimate for the whole region south of 35°S shows a strong positive CO_2 flux trend in the 1990s [Le Quéré et al., 2007] and a strong negative CO_2 flux trend, reinvigorating the carbon sink in the 2000s [Landschützer et al., 2015] (fig. 4). The modeled σ_{DIV} is lower than of the decadal variations of SOM-FFN. The decadal variability σ_{DIV} in SOM-FFN data is 0.35 PgC, with the most positive CO_2 flux trend in the 1990s of +0.40 PgC and the most negative trend of -0.72 PgC . These values of σ_{DIV} suggest that these magnitudes in trends could be due to internal variability with a probability of 5% ($\sim 2\sigma$) and 0.2% ($>3\sigma$) for 1990s and 2000s trends respectively. This outlines how unlikely these observed CO_2 flux trends can be attributed to internal variability from the perspective of numerical modeling.

The modeled internal variability of an interactive carbon cycle would be a more realistic counterpart for the observed internal variability, as the MPI-ESM LE simulations are forced with prescribed atmospheric CO_2 concentrations. The internal variability with an interactive carbon cycle produces 25% higher internal variability because of the non-linear changes in atmospheric CO_2 concentrations due to terrestrial carbon uptake [Ilyina et al., 2013].

Highlighted monotonic CO₂ flux trends I select the most extreme positive and negative monotonic trends. Applying this selection criteria, I highlight two extreme CO₂ flux trends in fig. 4. Analyzing a range of trendlengths from 6 to 14 years, I assess that MPI-ESM LE is able to capture positive and negative multi-year and decadal CO₂ flux trends in the Southern Ocean (Fig. A.2). For decadal 10-year trends, the most extreme cases are of the same magnitude as those observed in the 1990s and 2000s [Le Quéré et al., 2007, Landschützer et al., 2015] (Fig. A.2).

I choose extreme monotonic trends to study the processes driving internal variability in the carbon cycle because stronger trends will give me a stronger signal in the underlying processes, which are discussed in chapter 4.

Comparison of ensemble CO₂ flux internal variability This is in contrast to other perturbed initial conditions large ensembles (see section 2.2). Neither CESM LE nor GFDL LE can reproduce similar strong decadal CO₂ flux trends in the Southern Ocean [personal communication Nikki Lovenduski, Sarah Schlunegger]. McKinley et al. [2016] mentioned a weak carbon sink for CESM LE. Resplandy et al. [2015] showed that MPI-ESM's dominant area of internal variability is the Southern Ocean, whereas CESM is most variable in the tropical and Indian Pacific and GFDL LE has large internal variability in tropical Indian Pacific as well as the Southern Ocean.

The different method of initialization could not have caused the behavior of trends, because the CO₂ flux pathways of different realizations already cross after few years and upper ocean loses his history after 50 years. The internal variability specific to the model itself is dominating [Lovenduski et al., 2016].

3.2 Winds

Spatial distribution in the mean state Winds are governed by distributions in sea-level pressure. They point from high pressure to low pressure systems, but get diverted to their left in the Southern hemisphere by the Coriolis force. Therefore, strong westerly winds are established between the low-pressure system south of 45°S and higher pressure systems over the subtropical gyres (fig. 5a). This is zonally symmetric SLP pattern in the ensemble climatological mean leads to zonally symmetric westerly winds peaking at 50°S and decaying further northwards.

Spatial mean comparison to observational data The spatial zonal distribution in observational data from a NCEP reanalysis climatology is so similar to the MPI-ESM LE climatology that I plot the difference between MPI-ESM LE climatology and NCEP reanalysis [Kalnay et al., 1996] (fig. 5c). The position of the jets in ECHAM is shifted to lower latitudes [Stevens et al., 2013] which seems to be a common atmospheric modeling challenge [Kidston and Gerber, 2010]. Therefore, the modeled westerlies are too strong from 30-60°S and too weak south of 60°S. The zonal wind speed difference peaks at 45°S at +1m/s.

Spatial distribution of internal variability The decadal internal variability σ_{DIV} increases zonally towards lower latitudes with the highest internal decadal variability in the pacific sector in the Southern Ocean seasonal ice-covered area (fig. 5b).

Spatial internal variability comparison to observational data Observational reanalysis data reveal the same spatial distribution with a higher amplitude of decadal internal variability (fig. 5d). The pacific sector reflects the area of an Antarctic dipole induced from the El Niño-Southern Oscillation (ENSO), which manifests itself in variability of sea-ice [Yuan, 2004]. This is also known as the Pacific-South American (PSA) Oscillation [?]. The atmospheric Southern Ocean jet splits and in El Niño conditions intensifies on a northern route which induces a low pressure system with more storms. La Niña conditions bring a high pressure system with less storms vice versa. Such tele-connections of the tropics into the Southern Ocean are subject of current research and rarely analyzed for the Southern Ocean carbon sink.

Temporal evolution of the mean state and internal variability Fig. 5 shows the temporal evolution and internal variability of the annual Southern Annular Mode (SAM) index calculated according to [Gong and Wang, 1999] (see section 2.5.1). Positive SAM index values are associated with anomalously a low sea-level pressure over Antarctica which result in a southward shift and intensification of westerly winds. The ensemble mean has a positive trend. This trend is a consequence to anthropogenic CO₂ emission and ozone depletion over Antarctica [Thompson and Wallace, 2000].

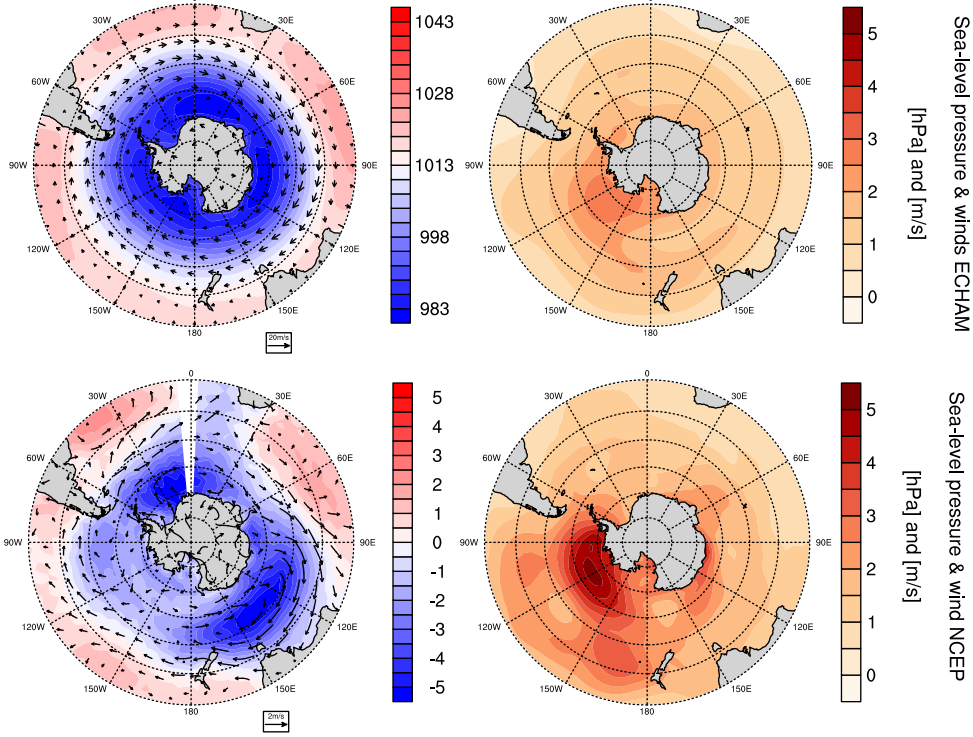


Figure 5: Spatial distribution of the Southern Ocean sea-level pressure and wind vectors overlain as arrows: ensemble mean climatology from 1980 to 2004 (a) as forced signal and ensemble decadal standard deviation (b) as decadal internal variability σ_{DIV} ; and the difference between MPI-ESM and reanalysis data from NCEP climatology [Kalnay et al., 1996] (c), and decadal internal variability σ_{DIV} from NCEP climatology (d).

Temporal comparison to observational data MPI-ESM LE SAM index lies in the range of the station-based from [Marshall, 2003], although it follows a weaker trend in the ensemble mean.

Temporal evolution of extreme carbon trend members The positive CO₂ flux trend shows a positive trend in SAM. Those strengthening winds increase upwelling (see section 3.4), which brings waters over-saturated in DIC to the surface and hence lead to outgassing anomalies. This weakens the carbon sink and vice versa strengthens the carbon sink under the context of weakening westerly winds. The detailed response of primary production and upwelling under the context of changing winds is discussed in chapter 4.

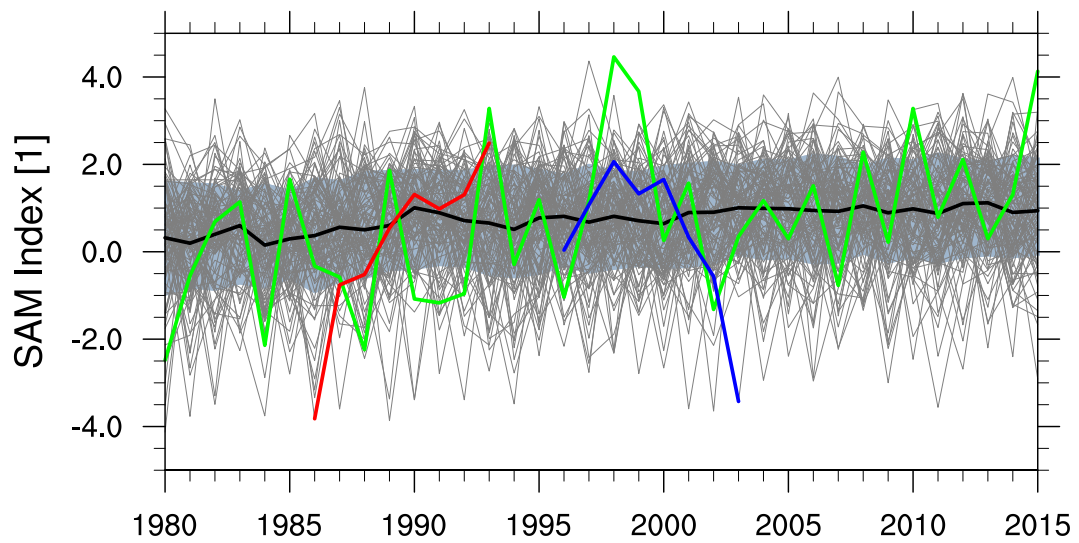


Figure 6: Temporal evolution of the annual Southern Annular Mode (SAM) index according to [Gong and Wang, 1999]. Grey lines show the 100 ensemble members; the black line the ensemble mean; the blue shading is the decadal internal variability σ_{DIV} ; the red line represents positive CO₂ flux trend; the blue line shows the negative CO₂ flux trend; the green line shows the station-based SAM from Marshall [2003]

3.3 Biology

Spatial distribution in the mean state (fig. 3a) The strong seasonal cycle in insulation and the sparseness of land topography leads to first-order zonally symmetric constraints for light and sea-surface temperature (SST). The high-latitude Southern Ocean is a so-called high nutrient low chlorophyll (HNLC) region, where light is the dominant limiting factor for the low biological production, but nutrients are plenty [Falkowski et al., 1998]. Summer sea-ice cover and sub-zero SST values constrain plankton growth and is responsible for the tiny amount of primary production in the coastal areas as well as the Ross Sea and Weddell Sea.

With decreasing latitude in the Southern Ocean, primary production increases along with increasing temperatures and light availability. Nutrients are upwelled by the upper-ocean overturning circulation and advected northwards by Ekman transport. This latitudinal increase of primary production peaks at 40-50°S, where nutrients are abundant from upwelling and Ekman transport and higher temperatures and light availability foster phytoplankton growth rates. The mixing with warm subtropical waters off the Argentinian coast increases SST and leads to a maximum primary production in the Southern Ocean [Behrenfeld, 2014]. Downstream the Drake passage, the polar front with its cold waters extends more northward [Orsi et al., 1995]. Along with lower nutrient concentrations due to increased precipitation from storms explains the relatively low primary production in the Atlantic sector compared to other longitudinal counterparts.

At the subtropical front, decreasing nutrient concentrations limit primary production [Behrenfeld, 2014].

Spatial mean comparison to observational data To evaluate HAMOCC's ability to model the Southern Ocean, I do not compare modeled primary production to chlorophyll-a concentration derived from satellite data, because satellite images are frequently hidden by clouds. Instead, I compare the distributions of nitrate which is the limiting nutrient for biological production in this HAMOCC version. The distribution of nitrate shows a strong gradient in HAMOCC as well as in the World Ocean Atlas (WOA) 2013 [Garcia et al., 2013] along the fronts from low-nutrients in the high-latitudes to nutrient depletion in the subtropical gyres (fig. 8). In higher latitudes HAMOCC underestimates the phosphate concentration by 25%. These lower nutrient concentrations can be a sign of more nutrient consumption at higher primary production or be the reason for lower primary production. The distribution of another important nutrient phosphate shows a similar spatial pattern (fig. A.5).

Spatial distribution of internal variability Internal decadal variability in vertically integrated primary production in the Southern Ocean is higher in high productivity areas (fig. 7b). The whole region at 45-60°S, especially in the Indian sector, shows a enormously high decadal internal variability σ_{DIV} relative to the ensemble mean state. Internal vari-

ability in the Southern hemisphere is mostly driven by westerly winds. The explicit effect of those on HAMOCC is discussed in chapter 4.

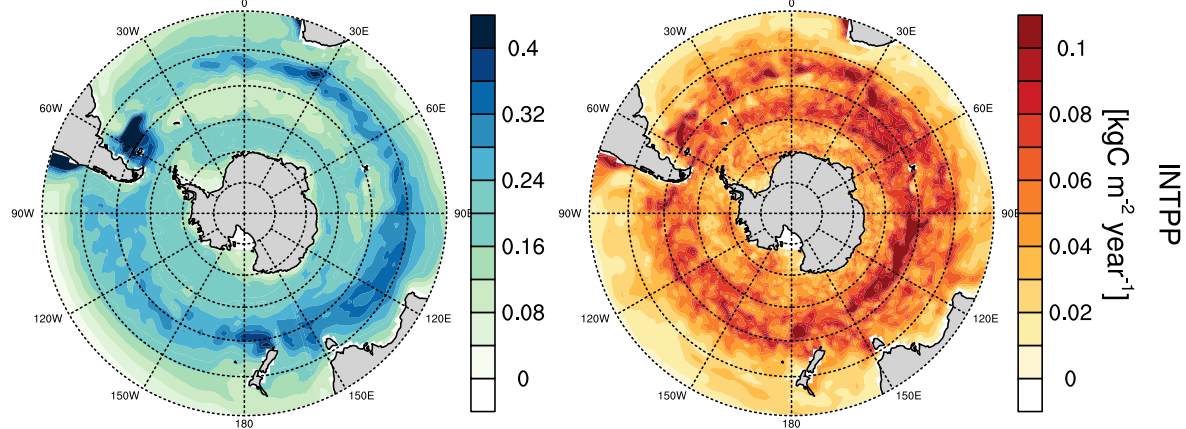


Figure 7: Spatial distribution of the vertically integrated primary production in the Southern Ocean: climatological ensemble mean from 1980 to 2004 (left) as forced signal and ensemble decadal anomaly standard deviation (right) as decadal internal variability σ_{DIV}

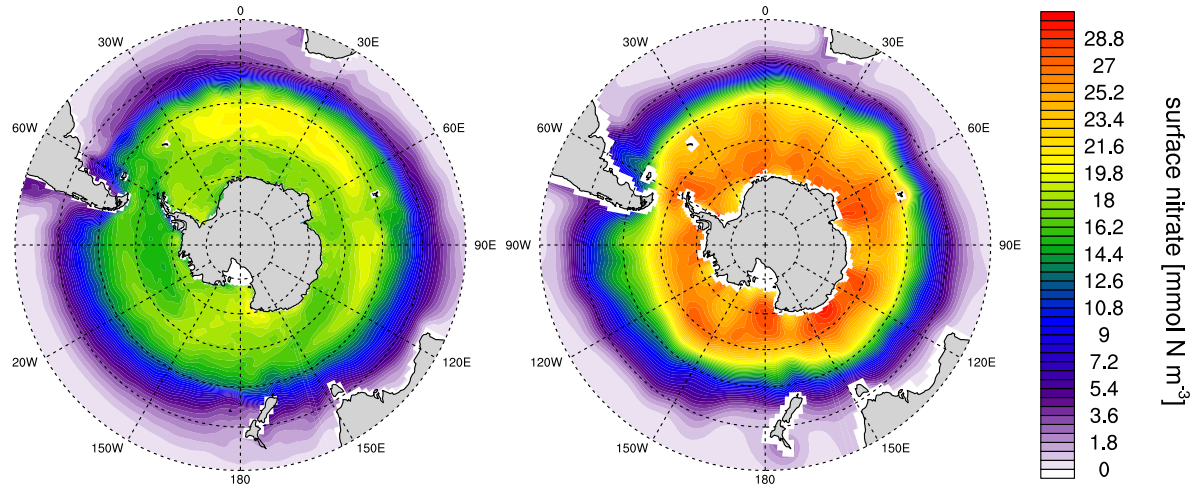


Figure 8: Spatial distribution of the climatology of surface nitrate (left) compared with WOA data [Garcia et al., 2013] (right)

Temporal evolution of the mean state and internal variability Primary production in the Southern Ocean is not subject to a strong forced trend in the historical period, but varies internally (fig. 9). The weak decreasing trend might be the first signs of increased stratification due to sea-surface warming, which in turn inhibits the mixing of nutrients. But the long-term consequences for primary production is subject to ongoing research and debate [Bopp et al., 2013, Taucher and Oschlies, 2011, Lozier et al., 2011, Kessler and Tjiputra, 2016, Krumhardt et al., 2017]. The decadal internal variability σ_{DIV} is 0.5 PgC.

The absolute amount of primary production exceeds CO₂ flux by a factor of \sim 20. The spatial distribution of export flux at 90m, which is the particulate organic matter that sinks below the euphotic zone before being remineralized, is the same as for primary production. As a lower vertical boundary for a upper-ocean carbon budget of the euphotic zone, export flux is of similar magnitude as CO₂ flux and thus comparable, see chapter 5.

Temporal evolution of extreme CO₂ flux trends The negative CO₂ flux trend has a positive trend in primary production, because primary production lowers surface DIC, pCO_{2,ocean} and hence reduces CO₂ uptake by the ocean; and vice versa negative trends in primary production lead to positive CO₂ flux trends.

HAMOCC Southern Ocean performance MPI-ESM is able to model the general features of the Southern Ocean, such as the characteristics of a high nutrient low chlorophyll region [Bopp et al., 2013]. But compared to other models and observational data, the seasonal cycle of phytoplankton blooms is amplified and too early in the Southern Ocean [Bopp et al., 2013, Nevison et al., 2016]. The reason of this is under current debate in the MPI biogeochemistry research group. It could involve that the Southern Ocean in MPI-ESM LE run is not iron-limited. Furthermore, the atmospheric bias in westerly winds and the Southern Ocean warm bias [Jungclaus et al., 2013] hinders sea-ice to propagate more extensively. A proper representation of Antarctic sea-ice would come along with a cooler, more stratified Southern Ocean which modulates primary production.

Additionally, the longest standing data records, which are on the northern hemisphere in Iceland [Six and Maier-Reimer, 1996], are used for the tuning of free model parameters. The Southern Ocean has never been in the focus of HAMOCC.

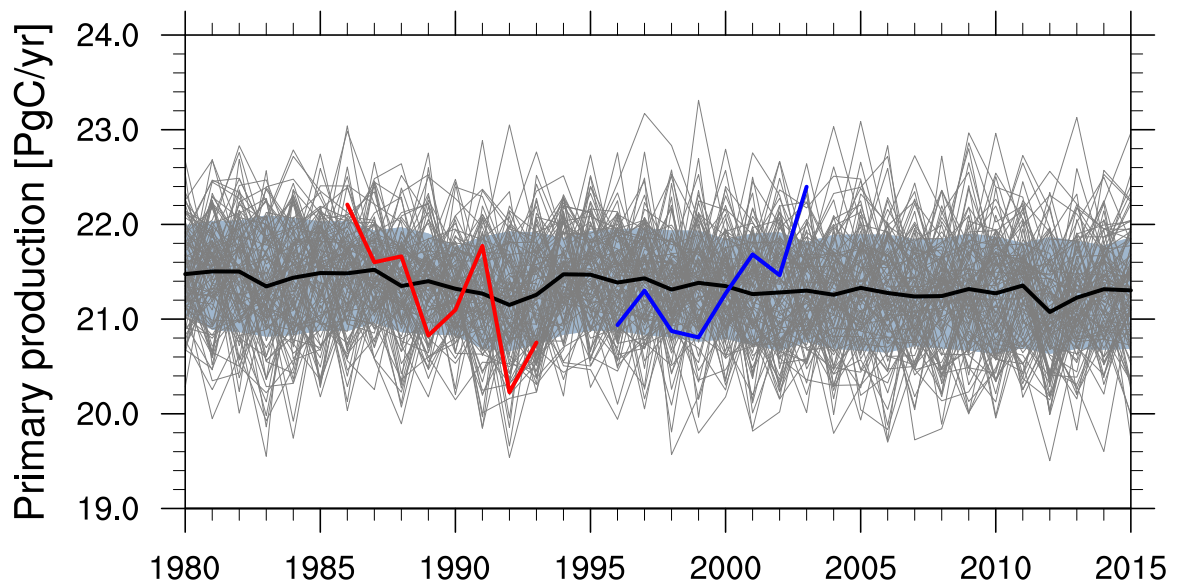


Figure 9: Temporal evolution of the vertically integrated primary production in the Southern Ocean south of 35°S . Grey lines show the 100 ensemble members, the black line the ensemble mean, the blue shading is the decadal internal variability σ_{DIV} , the red line represents the positive CO_2 flux trend, the blue line represents negative CO_2 flux trend

3.4 Upper-Ocean Overturning Circulation

Spatial distribution in the mean state and internal variability The Southern Ocean upper-ocean overturning circulation is driven by the divergence at 40-60°S corresponding to strong westerly winds. Fig. 10a shows a zonal transect view of the ensemble mean circulation. The isopycnals, which separate water masses, orient themselves at values from [Sallée et al. \[2013b\]](#), but are shifted to fit to typical depths, which is a common feature in water mass comparison as models have different density biases [[Sallée et al., 2013b](#)]. In the high latitudes south of 50°S, Ekman pumping brings Circumpolar Deep Water (CDW) from the ocean interior to the surface. At the surface, these waters are transported to the north. At lower latitudes, the surface waters warm and evaporation increases, so relatively cold and low salinity waters known as Antarctic Intermediate Water (AAIW) slide below warmer and more saline Subantarctic Mode Waters (SAMW) to extend northwards at intermediate depth. This process is called downwelling or Ekman subduction.

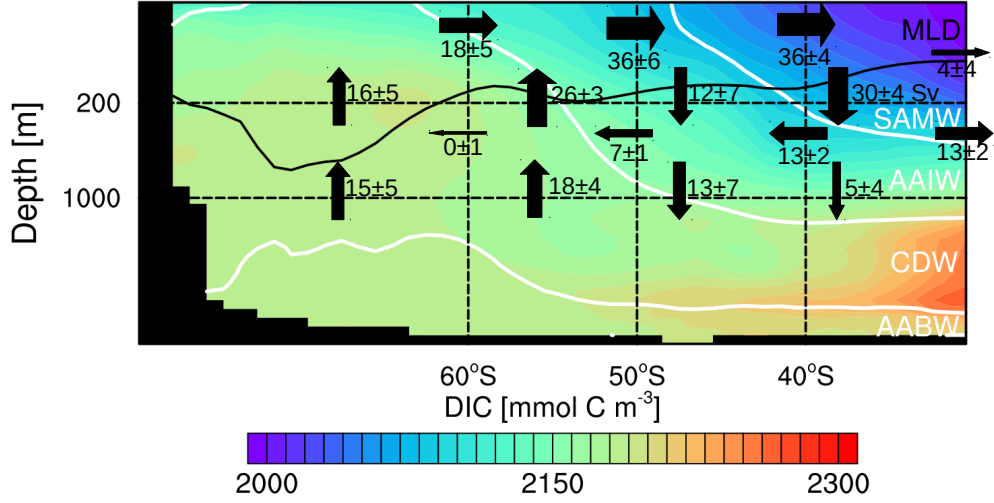
The strong upper-ocean circulation features upwelling south of 50°S, northward transport at 40-60°S and downwelling at 30-40°S and is known as the Deacon cell [[Döös and Webb, 1994](#), [Speer et al., 2000](#)]. The upper-ocean overturning circulation is driven by the strength and positions of westerly winds. Upwelling steepens and downwelling straightens the isopycnals along which the water masses flow. The internal variability in the horizontal processes at intermediate depth is lower than at the surface, because the influence of winds decays with depth. The decadal internal variability σ_{DIV} of vertical Ekman pumping and subduction is of similar magnitude at 200m and 1000m (fig. 10).

Comparison to observational data Fig. 10a is similar to Fig. 1 from [DeVries et al. \[2017\]](#) which uses observational data in an inverse model to demonstrate upper-ocean overturning circulation. Due to different vertical velocity regimes, I choose different boundaries for the transport, which prevents me from quantitative comparisons. Nevertheless, data of [DeVries et al. \[2017\]](#) Fig. 1 show the main characteristics of the Deacon cell and water transport of comparable magnitude as in MPI-ESM LE.

Link to the carbon cycle The concentration of dissolve inorganic carbon (DIC) in general increases with depth due to the biological pump and remineralization at depth. This is most clearly seen in the subtropics and blurred by all processes of mixing at higher latitudes (fig. 10). Still, upwelled waters from the deep oceans have a high pCO₂ potential at which they would equilibrate when lifted to the surface, so the upwelling super-saturated waters in high latitude waters drives CO₂ outgassing and downwelling takes CO₂ equilibrated waters into the deeper ocean (fig. 10b).

Trends of extreme carbon trend members The positive CO₂ flux trend shows intensified upper-ocean overturning circulation. This means enhanced upwelling, which

a



b

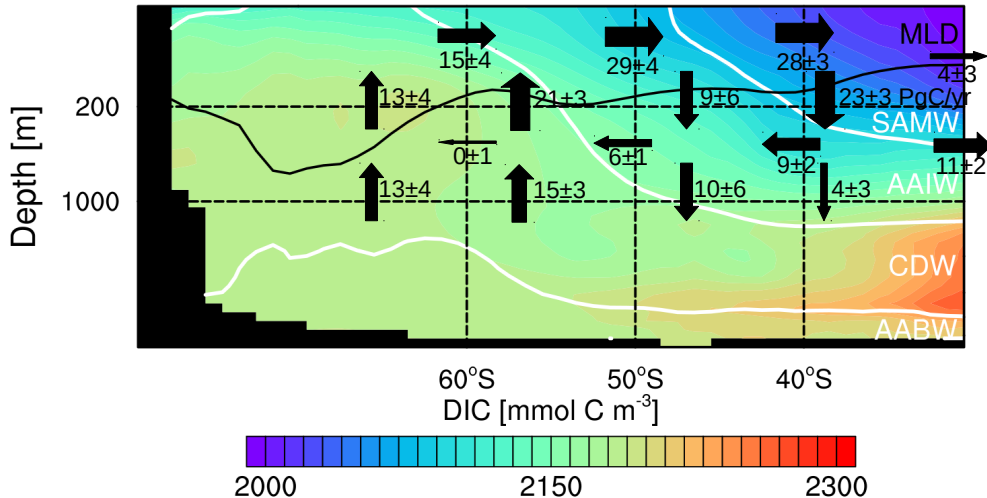


Figure 10: Zonally averaged transect of the Southern Ocean and the upper-ocean overturning circulation; black arrows show yearly mean advective transports of water in Sv (a) and carbon in PgC/yr (b) and its decadal internal variability σ_{DIV} ; white lines are isopycnals separating Sub-Antarctic Mode Water (SAMW) at potential density $\rho_\theta = 1026.5 \text{ kg m}^{-3}$ from Antarctic Intermediate Water (AAIW), at $\rho_\theta = 1027.2 \text{ kg m}^{-3}$ from Circumpolar Deep Water (CDW), at $\rho_\theta = 1027.7 \text{ kg m}^{-3}$ from Antarctic Bottom Water (AABW); the black line is the mixed-layer depth (MLD); the colored contours show the distribution of dissolved inorganic carbon (DIC)

weakens the carbon sink (Fig. 21) and vice versa strengthen the carbon sink for weaker upper ocean overturning circulation (fig. 16).

MPI-OM Southern Ocean performance evaluation The global performance of MPIOM is discussed in detail in [Jungclaus et al. \[2013\]](#). The Southern Ocean sea-surface temperature warm bias is attributed to an overestimation of downward shortwave radiation into the polar regions [[Stevens et al., 2013](#)] and causes the underestimation of sea-ice coverage. Additionally, through open-ocean convection in the Ross and Weddell Sea and deeper than observed winter mixing, heat from the relatively warm circumpolar deep waters warm the subsurface waters [[Stössel et al., 2015](#)]. Additional freshwater input from melting glaciers distributed along the coast a basal meltwater and along the high-latitude Southern Ocean to mimic freshwater input due to icebergs would improve the water column stability to prevent open-ocean convection. The same effect would have the coupling to a higher resolved atmosphere due to additional freshwater input [[Stössel et al., 2015](#)].

The model quality of overturning circulation in the Southern Ocean is analyzed by [Sallée et al. \[2013b\]](#). MPI-ESM realistically simulates subtropical water temperature and SAMW in general. But the overturning cell is much weaker than in other models.

The mixed-layer depth (MLD) is an important measure to assess how climate models represent the Southern Ocean. MLD in MPI-ESM is overestimated compared to observational data from NOAA Atlas [[Monterey and Levitus, 1997](#)]; spatially in the locations of the ACC and the Ross and Weddell Sea (fig. 11) as well as in the zonal average (fig. 10). In the Ross and Weddell Sea, the MLD deepens to few kilometers depth via open-ocean convection [[Stössel et al., 2015](#)], which often appears in climate models but rarely seen in observations [[Heuzé et al., 2013](#)]. This and the weak stratification explains why MPI-ESM overestimates MLD in winter [[Sallée et al., 2013a](#)].

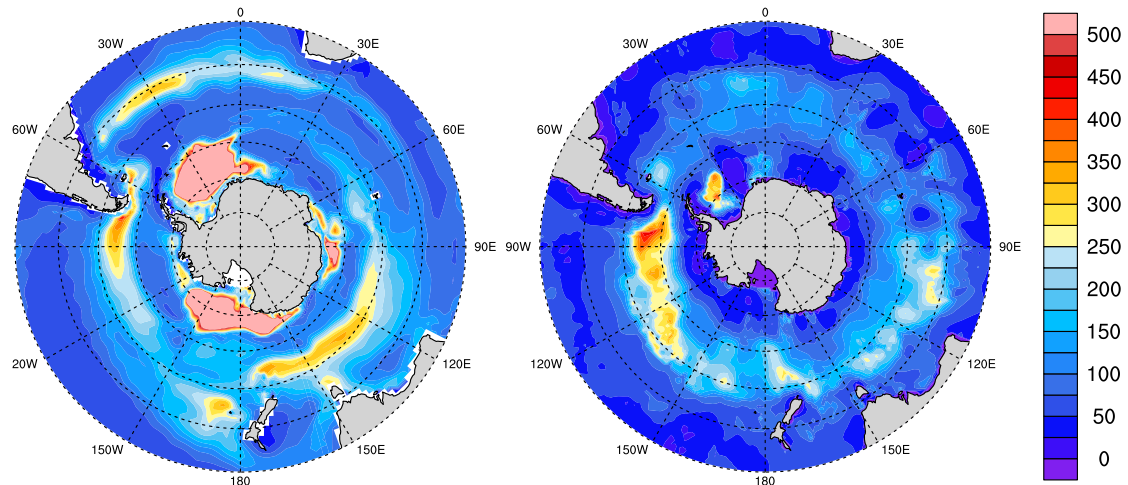


Figure 11: Spatial distribution of the ensemble mean climatology (1980-2004) of the mixed-layer depth (MLD) (left) compared with [Monterey & Levitus, 1997](#) NOAA Atlas

4 Trends in CO₂ flux

4.1 Winds determine internal variability of the Southern Ocean CO₂ flux

I find a correlation on 8-year trends between SAM, which describes the position and latitudinal shift of westerly winds, and the CO₂ flux in the area of largest decadal internal variability at 50-60°S (fig. 12). Although the CO₂ flux formula depends on the wind speed at 10m height, figure 12 emphasizes the importance and the changes in ΔpCO₂. However, the magnitude of short-term variability on the timescale of days to hours depends highly on wind strength variability, but the direction of CO₂ flux is independent of wind speed. This relationship reveals two distinct regimes of wind-driven CO₂ flux signals in this area:

Intensified and southward shifted winds, associated with an increasing trend in SAM, lead to a positive CO₂ flux trend. This Southern Ocean carbon sink response has been suggested frequently for the observed and projected trend in SAM [Le Quéré et al., 2007, Lovenduski et al., 2007, 2008, Hauck et al., 2013]. The related processes associated stronger winds are explained in section 4.2.

In MPI-ESM we also find the reverse case of weakening and northward shifting winds, associated with a negative trend in SAM, which lead to a negative CO₂ flux or ocean uptake trend. The related processes associated weaker winds are explained in section 4.3. However, observations do not reveal strong multi-year negative SAM trends (see fig. 6). Likewise, westerly winds did not weaken but continued to increase during the negative CO₂ flux trend in the 2000s [Landschützer et al., 2015].

To qualitatively understand the mechanisms of the Southern Ocean carbon sink, I analyze the drivers of CO₂ flux on a process level. This chapter covers CO₂ flux changes with respect to the thermal effect, physical circulation and biology. A quantitative analysis of the different drivers for different regions discussed in chapter 5.

The analysis presented here involves 8-year trends for reasons stated in section 2.4.2, but the results of this chapter apply to various multi-year trends subject to internal variability (not shown).

The spatial trend patterns of different trend periods appear zonally symmetric, therefore the analysis is not separated into the different Southern Ocean sectors, e.g. Pacific, Indian or Atlantic. Also, the atmospheric circulation change in models are too symmetric compared to observations [Haumann et al., 2014]. Therefore, the description here is carried out in zonal latitudinal bands keeping the unsymmetrical Southern Ocean dynamics in mind [Sallée et al., 2010, Talley, 2013]. Also due to the underestimated Antarctic sea-ice and open-ocean convection in the Ross and Weddell Sea, I restrict my analysis to the Southern Ocean north of 60°S, but the decadal CO₂ flux trends have a weak signal south of 60°S anyway.

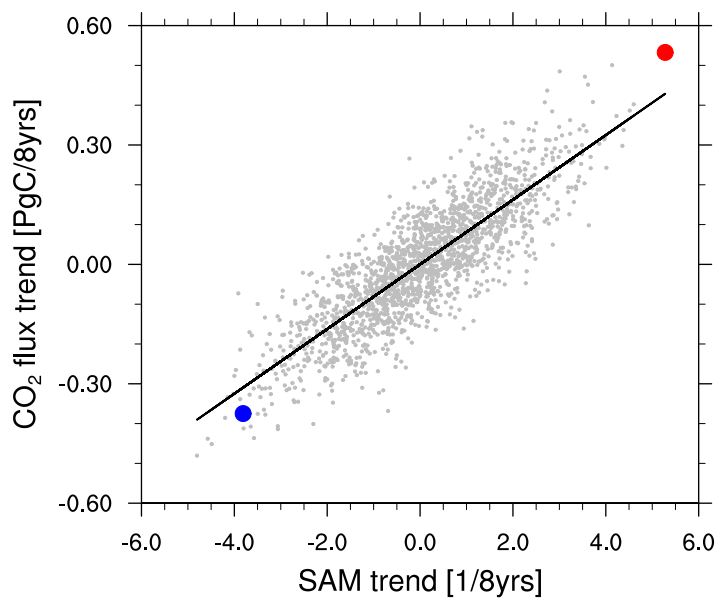


Figure 12: Linear trends in the Southern Annular Mode (SAM) as indicator of wind strength vs. CO₂ flux at 50-60°S; each data point represents 8-year trends of a single realization normalized for the ensemble mean trend between 1980 and 2005; the blue dot is the most negative monotonic CO₂ flux trend; the red dot is positive monotonic CO₂ flux trend.

4.2 Positive CO₂ flux trends

Strong positive CO₂ flux trends correlate with stronger westerly winds (fig. 12). The difference $\Delta p\text{CO}_2$ between oceanic $p\text{CO}_{2,\text{ocean}}$ and atmospheric partial pressures $p\text{CO}_{2,\text{atm}}$ depicts a cleaner signal than CO₂ flux and is independent of wind speed. $p\text{CO}_{2,\text{ocean}}$ rises stronger than $p\text{CO}_{2,\text{atm}}$, so CO₂ must be driven by changes in the ocean dynamics (fig. 13a). The strongest positive signal occurs in the upwelling at 50-60°S, a weaker and more patchy signal occurs in the subduction areas north of 50°S, whereas changes in most other areas of the Southern Ocean are insignificant (fig. 13a).

Westerly winds decrease at 40-50°S and increase at 50-60°S which results in a southward shift of westerlies (fig. 13b) represented by the positive trend in SAM (see fig. 6).

The response of the thermal effect, upper-ocean overturning circulation and biology are described in sections 4.2.1, 4.2.2 and 4.2.3, respectively.

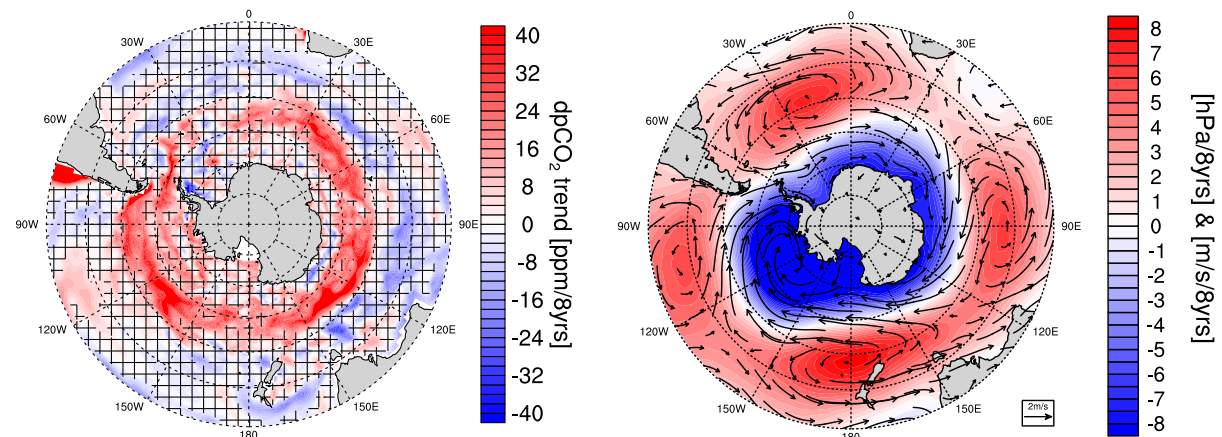


Figure 13: Linear trends in $\Delta p\text{CO}_2$ (left) and sea-level pressure and wind vectors overlaid as arrows (right) for the case of the most positive monotonic 8-year CO₂ flux trend; hatched areas indicate where trends are outside the 5% significance level

4.2.1 Changes in the thermal effect in positive CO₂ flux trends

The difference between the partial pressure of CO₂ in oceanic pCO_{2,ocean} and atmospheric pCO_{2,atm} is the main changing quantity in the CO₂ flux formula. The separation by [Takahashi et al. \[2002\]](#) gives insights about the direct influence of sea-surface temperatures (SST) (see section 2.5.2). The thermal pCO₂ trend is driven by changes in SST (fig. 14a), whereas the non-thermal trend includes changes in pCO_{2,atm}, biology, alkalinity, at constant SST (fig. 14b). The thermal trend and non-thermal trend approximately add up to the trends in pCO₂ [[Landschützer et al., 2015](#)].

The thermal trend follows the SST cooling trend (fig. A.7) south of 50°S towards negative CO₂ flux trends, whereas the warming north of 50°S favors outgassing. Increased Ekman transport causes this heat divergence in polar regions and a heat convergence at lower latitudes, which cause this response in the thermal pump [[Hall and Visbeck, 2002](#)] (see fig. 16). The non-thermal component strongly increases south of 50°S, so overall the pCO_{2,ocean} increases faster than pCO_{2,atm}, which leads to a positive CO₂. This reflects the enhanced outgassing from increased upwelling. The non-thermal and thermal trends combined nearly compensate north of 50°S, but at 50-60°S the outgassing dominates (fig. 13a). The homogenous increase in atmospheric pCO_{2,atm} accounts for a -12ppm/8yrs in fig. 13b. These changes are stronger in the summer season, especially the non-thermal component (see fig. A.9, A.10).

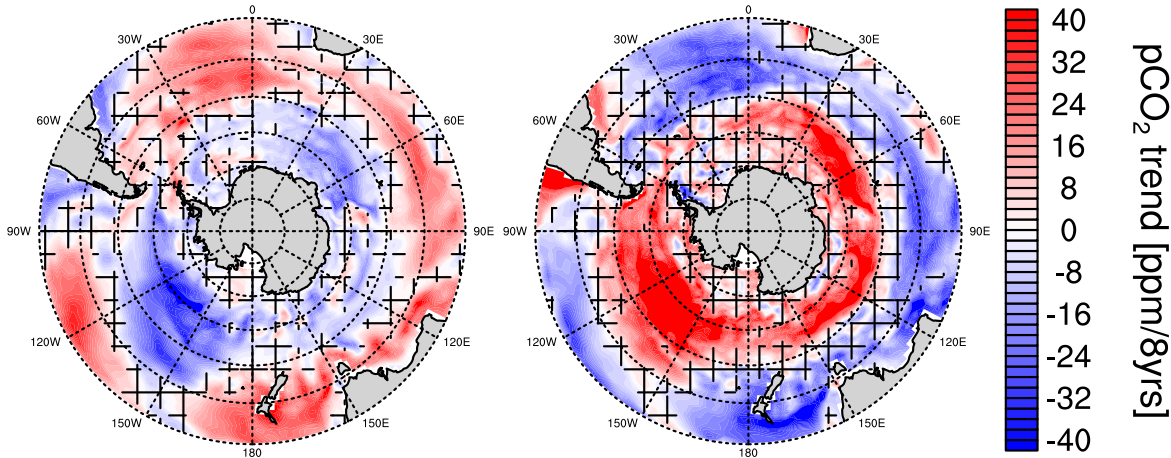


Figure 14: Linear trends in pCO_{2,thermal} (left) and $\Delta p\text{CO}_{2,\text{non-thermal}}$ (right) for the case of the most positive monotonic 8-year CO₂ flux trend; hatched areas indicate where trends are outside the 5% significance level

4.2.2 Changes in ocean circulation in positive CO₂ flux trends

Stronger westerly winds intensify the upper-ocean overturning circulation [Lauderdale et al., 2013]. The circulation field advects DIC along its overturning pathway (fig. 16). Intensified upwelling of carbon-rich waters 50-60°S increases DIC concentrations in the euphotic zone (fig. 15b). An over-saturation in DIC leads to a positive CO₂ flux. The stronger winds also increase Ekman northward transport and advects DIC further northward (fig. 15a). North of 50°S, subduction rates of AAIW and SAMW formation increase, so pCO_{2,atm}-equilibrated waters take additional anthropogenic carbon into the deeper ocean. The southward shift of westerly winds weakens the northern edge of Ekman transport at 30-40°S.

The changes in mixed-layer depth (MLD) also contribute to the vertical transport of carbon. By deeper mixing in winter, more carbon-rich waters are included in the MLD, which then serves as a larger reservoir of super-saturated DIC. MLD deepens south of 50°S and slightly shoals north of 45°S, whereas open-ocean convection causes the unrealistic zonal MLD averages below 300m south of 60°S (fig. 16) ([Sallée et al., 2013a, Stössel et al., 2015]).

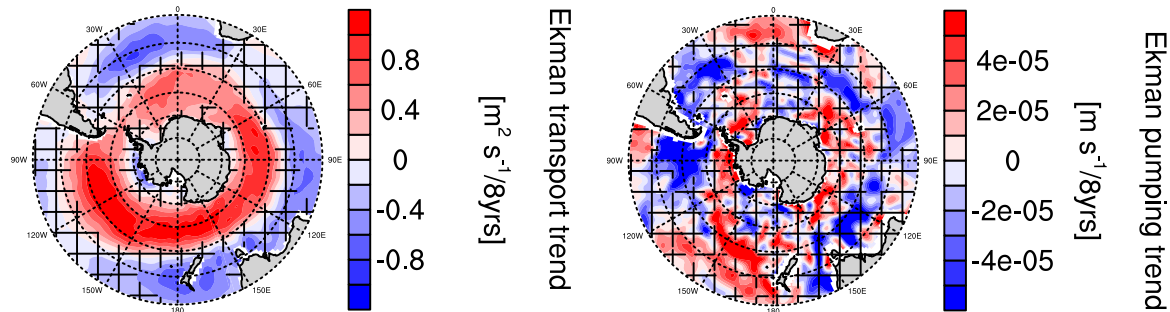


Figure 15: Linear trends in Ekman transport and Ekman pumping in the case of the most positive 8-years CO₂ flux trend; hatched areas indicate where trends are outside the 5% significance level

The upper-ocean overturning circulation response presented here is in line with idealized wind-change studies [Lauderdale et al., 2013], modeling studies explaining the observed CO₂ flux trend in the 1990s [Le Quéré et al., 2007, Lovenduski et al., 2007, 2008], as well an inverse modeling study for the 1990s [DeVries et al., 2017].

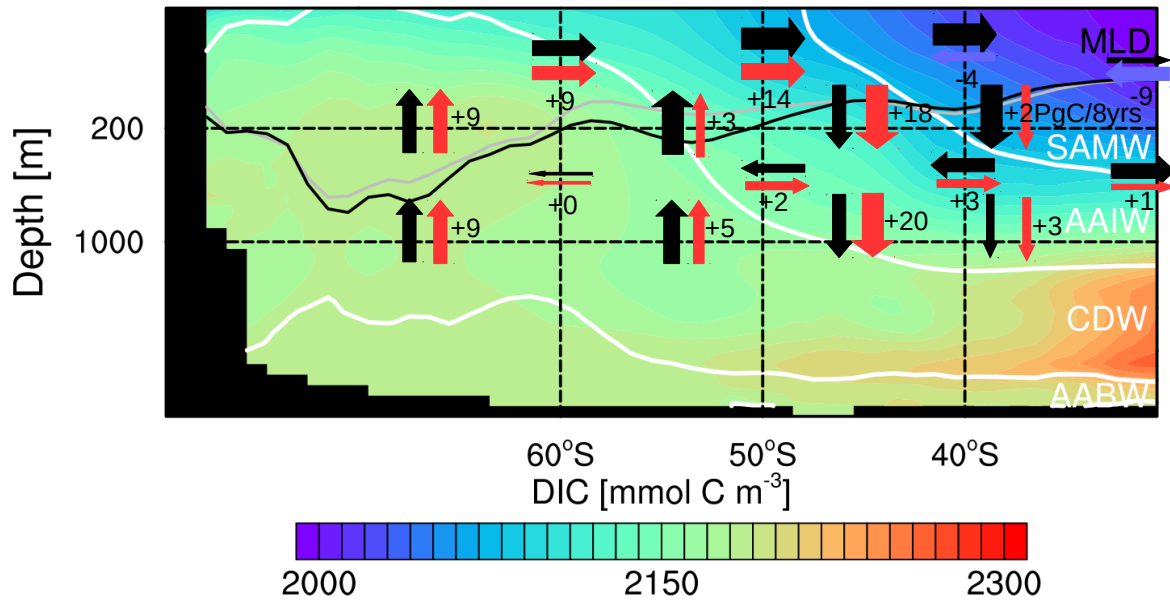


Figure 16: Zonally averaged upper-ocean overturning circulation in the case of the most positive 8-year CO_2 flux trend; black arrows show mean advective carbon transport, red arrows show positive advective carbon transport trends; blue arrows show negative advective carbon transport trends; black numbers quantify the trends in advective carbon transport in PgC/8yrs ; white lines are isopyncals as in fig. 10; grey line is mixed-layer depth (MLD) in the beginning and the black line MLD in the end of the period.

4.2.3 Changes in biology in positive CO₂ flux trends

The biological pump draws down surface DIC and is sensitive to changes in circulation (see section 2.1.3). In this subsection, I analyze the 8-year summer (SONDJF) austral summer trends of quantities related to primary production.

Primary production and CO₂ flux show opposing zonally symmetric trend patterns as phytoplankton growth takes up large amounts of surface DIC and hence lowers pCO₂ (fig. 17a,b). Primary production declines most pronounced at 50-60°S, increases at 40-50°S and declines at 30-40°S. Why?

Internal variability might change the availability of nutrients. The decline in nutrients in the subtropics at 30-40°S reduces primary production, but the nutrient availability factor (for definition see 2.1.3) slightly increases south of 50°S (fig. 17c). Previous observational and modeling studies suggest an increase in primary production, because upwelling brings nutrients, especially iron, from the deep-ocean to the iron-limited surface waters [Lovenduski and Gruber, 2005, Hauck et al., 2013, Wang and Moore, 2012, Tagliabue et al., 2014]. Additional iron fosters primary production following the iron-hypothesis [Martin et al., 1990, Martin, 1990], but observational data for iron is very sparse to test this for the whole Southern Ocean [Tagliabue et al., 2014]. Contrasting HAMOCC, many models reproduce this suggested iron-limitation in the Southern Ocean and hence respond with increase primary production [Wang and Moore, 2012, Hauck et al., 2013].

If the reduction in primary production at 50-60°S cannot be explained by changes in nutrients, what else effects primary production blooms?

The combined light & temperature limitation is primarily driven by temperature after the insulation excels a threshold in cold waters (see fig. A.13). A strong SST cooling trend comes along with stronger winds, because the increased Ekman transport pushes cold polar waters more northward (fig. A.7). The strong light & temperature limitation signal in coastal areas as well as Weddell and Ross Sea is attributed to sea-ice changes and open-ocean convection, but has minor effects on the primary production and CO₂ flux (fig. 17d).

This northward Ekman transport could also advect phytoplankton northwards to cause the increase in primary production at 40-50°S (fig. 15).

The overall decline of primary production in the Southern Ocean under a positive SAM trend is related to mixing: The summer mixed-layer depth (MLD) has a strong increasing trend at 50-60°S, so the mixing deepens (fig. 17e). This is caused by stronger winds (fig. 13b) and shown in the average depth of the vertical diffusivity due to wind (fig. 17f). This deeper mixing in summer then mixes the standing stock of phytoplankton to deeper levels, where they are exposed to less light (fig. 17g). This theory of a critical depth for phytoplankton blooms was proposed by Sverdrup [1953] and requires a stable water column for phytoplankton to initiate blooms. However, this theory is based on turbulent mixing, so the oceanographic MLD only serves as a first-order mixing measure

for phytoplankton [Franks, 2014]. Still the signal sustains to phytoplankton depth, where the average phytoplankton depth decreases up to 15m which results in up to 30% less light. The lack of monthly output for 3D biogeochemical variables made me use annual averages for phytoplankton, which causes the low significance in fig. 17g.

The reverse processes contributes to the increase at 40-50°S: Less winds mix less deep and allow phytoplankton to stay more confined to the surface, where they get more light and flourish (fig. 13b, 17e,f,g,b). Also the warming increases the phytoplankton growth rate (fig. 17d).

Summarizing, a multitude of interconnected processes causes the decline in primary production in the Southern Ocean for an increasing SAM trend. A clear separation of the magnitude of the different effects is impossible.

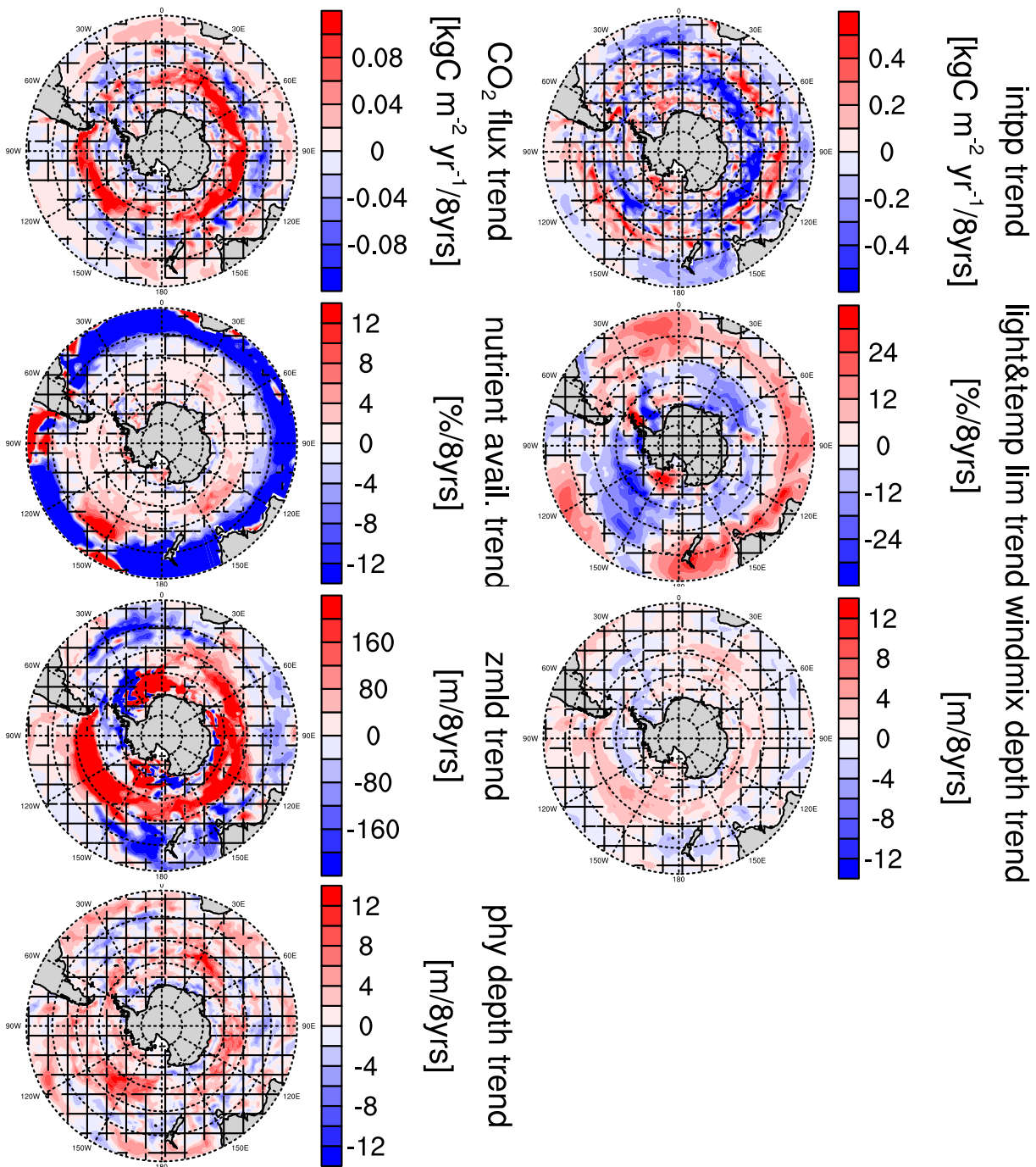


Figure 17: Southern Ocean austral summer trends for the case of the most positive 8-year CO₂ flux trend: CO₂ flux (a), vertically integrated primary production (b), nutrient availability factor (c), surface temperature & limitation function (d), mixed layer depth (e); average depth of vertical diffusivity due to wind (f) and phytoplankton average depth (g); hatched areas indicate where trends are outside the 5% significance level

4.3 Negative CO₂ flux trends

Disclaimer: Generally, trends in this analysis reverse for weaker compared to strengthening westerlies, which leads to an overall negative CO₂ flux trend. Additionally, now the prescribed atmospheric $pCO_{2,atm}$ forcing promotes a steady negative background CO₂ flux trend.

Strong negative CO₂ flux trends correlate with weaker westerly winds (fig. 18). The strongest negative signal ΔpCO_2 occurs in the upwelling at 50-60°S, whereas changes in most other areas of the Southern Ocean are insignificant (fig. 18a).

Westerly winds decrease at 40-60°S, which results in a northward shift of westerlies (fig. 13) represented by the negative trend in SAM (see fig. 6).

The response in the thermal effect, upper-ocean overturning circulation and biology are described in sections 4.3.1, 4.3.2 and 4.3.3, respectively.

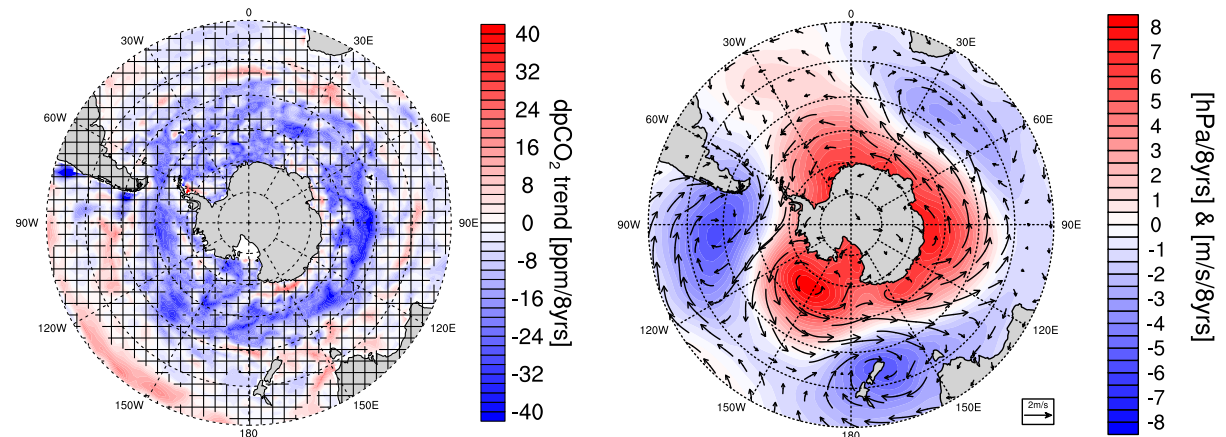


Figure 18: Linear trends in ΔpCO_2 (left) and sea-level pressure and wind vectors overlaid as arrows (right) for the case of the most negative monotonic 8-year CO₂ flux trend; hatched areas indicate where trends are outside the 5% significance level

4.3.1 Changes in the thermal effect in negative CO₂ flux trends

The thermal trend follows the SST warming trend (fig. A.8) south of 50°S towards positive CO₂ flux trends, whereas the cooling north of 50°S favors CO₂ uptake (fig. 19a). This is caused by a heat convergence in the polar region and a heat divergence in the subtropics caused by less Ekman transport [Hall and Visbeck, 2002]. The non-thermal trend is slightly positive north of 50°S and negative south of 50°S with the strongest signal in the areas of upwelling at 50-60°S (fig. 19b). The increase in atmospheric pCO_{2,atm} accounts for a -14 ppm/8yrs. The non-thermal and thermal trends combined nearly compensate north of 50°S, but the non-thermal component dominates at 50-60°S (fig. 18a).

These changes are stronger in the summer season, especially the non-thermal component (see fig. A.11, A.12).

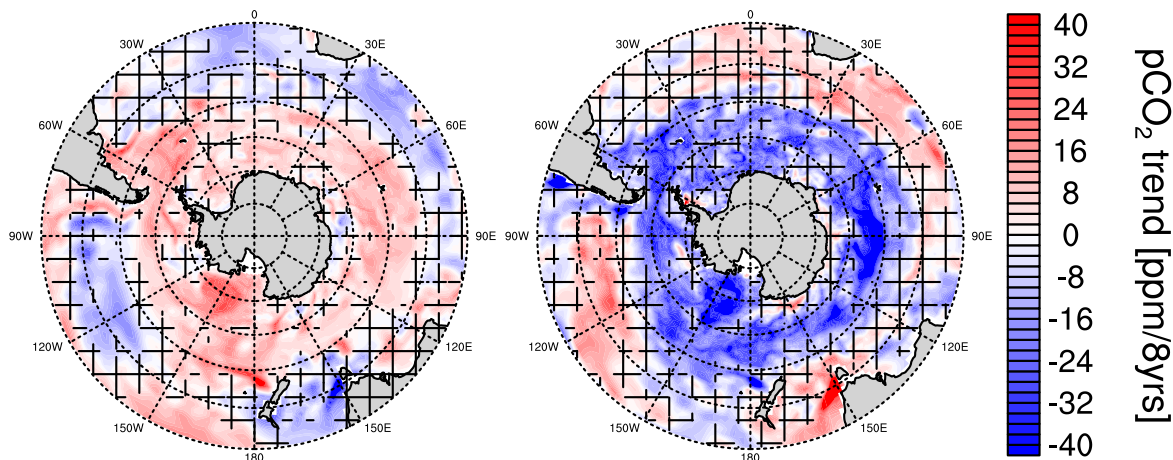


Figure 19: Linear trends in $p\text{CO}_{2,\text{thermal}}$ (left) and $\Delta p\text{CO}_{2,\text{non-thermal}}$ (right) for the case of the most negative monotonic 8-year CO₂ flux trend; hatched areas indicate where trends are outside the 5% significance level

4.3.2 Changes in ocean circulation in negative CO₂ flux trends

Weaker westerly winds slow down the upper-ocean overturning circulation [Lauderdale et al., 2013]. The circulation field advects DIC along its overturning pathway (fig. 21). Weaker upwelling of carbon-rich waters 50–60°S decreases DIC concentrations in the euphotic zone (fig. 20b). An under-saturation in DIC leads to a negative CO₂ flux. Weaker winds also decrease Ekman northward transport and advects DIC less northward (fig. 20a). North of 50°S, subduction rates of AAIW and SAMW formation decrease, so pCO_{2,atm}-equilibrated waters take less anthropogenic carbon into the deeper ocean. The northward shift of westerly winds strengthens the northern edge of Ekman transport at 30°S. MLD shoals south of 50°S and slightly deepens north of 45°S, whereas open-ocean convection causes the unrealistic zonal MLD averages below 300m south of 60°S (fig. 21).

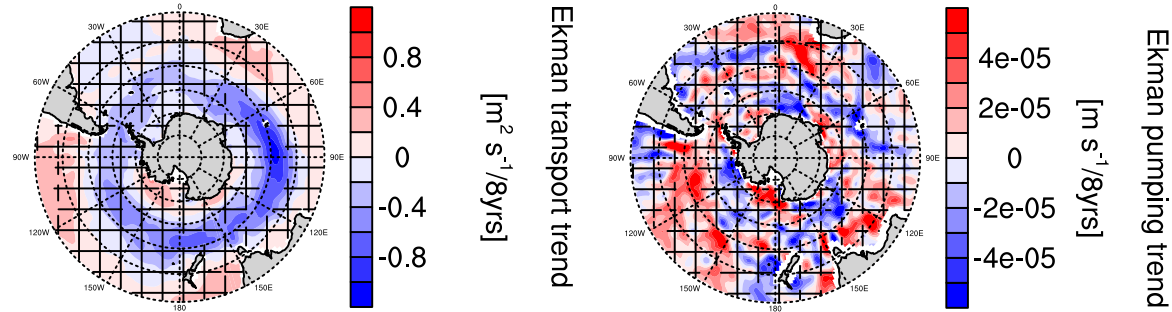


Figure 20: Linear trends in Ekman transport and Ekman pumping in the case of the most negative 8-years CO₂ flux trend; hatched areas indicate where trends are outside the 5% significance level

The upper-ocean overturning circulation response presented here is in line with idealized wind-change studies [Lauderdale et al., 2013]. The inverse modeling study reports a decline from the 2000s towards the previous decade [DeVries et al., 2017]. However, a negative trend for the strength of westerly winds has not been observed, but the patterns in sea-level pressure in the 2000s became more zonally asymmetric [Landschützer et al., 2015].

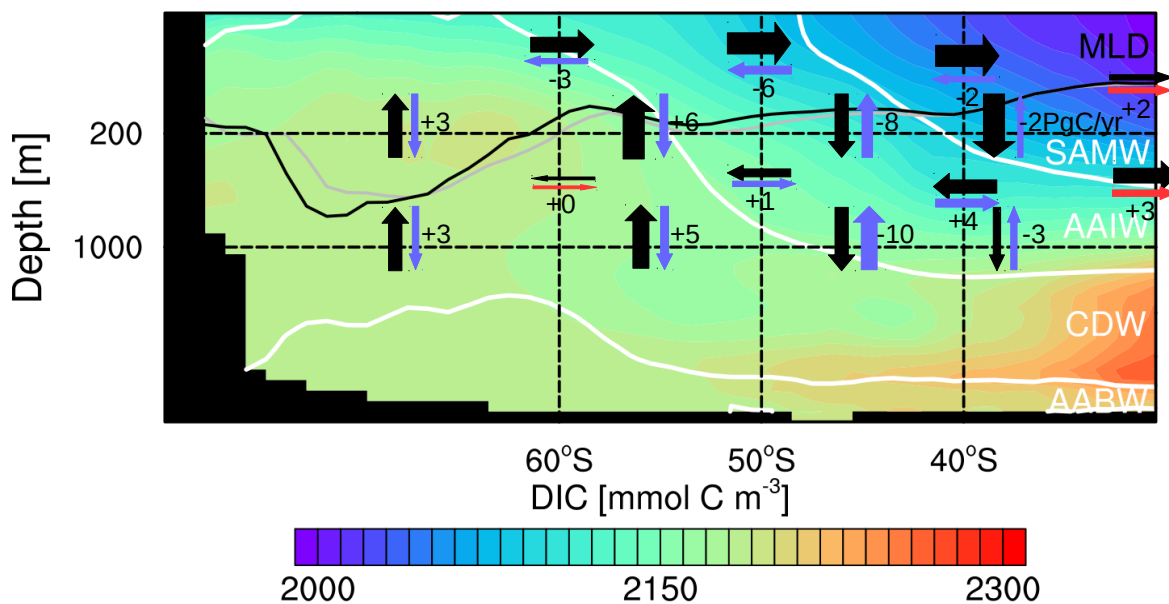


Figure 21: Zonally averaged upper-ocean overturning circulation in the case of the most negative 8-year CO_2 flux trend; black arrows show mean advective carbon transport, red arrows show positive advective carbon transport trends; blue arrows show negative advective carbon transport trends; black numbers show the trends in advective carbon transport in PgC/8yrs ; white lines are isopycnals as in fig. 10; grey line is mixed-layer depth (MLD) in the beginning and the black line MLD in the end of the period.

4.3.3 Changes in biology in negative CO₂ flux trends

Primary production and CO₂ flux show opposing zonally symmetric trend patterns as phytoplankton growth takes up large amounts of surface DIC and hence lowers pCO₂ (fig. 22a,b). CO₂ flux trend here also follows the atmospheric pCO_{2,atm} forcing. Primary production increases most pronounced at 50-60°S, decreases at 40-50°S and increases at 30-40°S. Why?

Internal variability might change the availability of nutrients. The increase in nutrients in the subtropics at 30-40°S fosters primary production, but nutrient availability factor slightly decreases south of 50°S (fig. 22c). Previous observational and modeling studies suggest an decrease in primary production because less upwelling brings less nutrients, especially iron, from the deep-ocean to the surface [Tagliabue et al., 2014]. But the Southern Ocean in HAMOCC is nitrate limited, so the slight nutrient depletion might originate in the increases nutrient consumption due to primary production.

If the reduction in primary production at 50-60°S cannot be explained by changes in nutrients, what else effects primary production blooms?

A strong SST warming trend comes along with weaker winds, because the increased Ekman transport pushes cold polar waters less northward (fig. A.8). The strong light & temperature limitation signal in coastal areas as well as Weddell and Ross Sea is attributed to sea-ice changes and open-ocean convection, but has minor effects on the primary production and CO₂ flux (fig. 22d).

The weakened northward Ekman transport could also keep the phytoplankton more southwards and cause the increase in primary production at 50-60°S and the shifted decrease at 40-50°S (fig. 20).

The overall increase of primary production in the Southern Ocean under a positive SAM trend is also related to mixing: The summer mixed-layer depth (MLD) has a strong decreasing trend at 50-60°S, so the mixing decreases (fig. 22e). Weaker winds (fig. 18b) mix the ocean less deep (fig. 22f). This reduced mixing in summer keeps the standing stock of phytoplankton in light-flooded levels, where they grow faster (fig. 17g). The reverse process contributes to the decrease at 40-50°S: Stronger winds mix deeper and draw phytoplankton down, where they get less light and grow less (fig. 13b, 17e,f,g,b). Additionally, the cooling slows down phytoplankton growth (fig. 22d).

Summarizing, a multitude of interconnected processes caused the increase in primary production in the Southern Ocean for a decreasing SAM trend. A clear separation of the magnitude of the different effects is impossible.

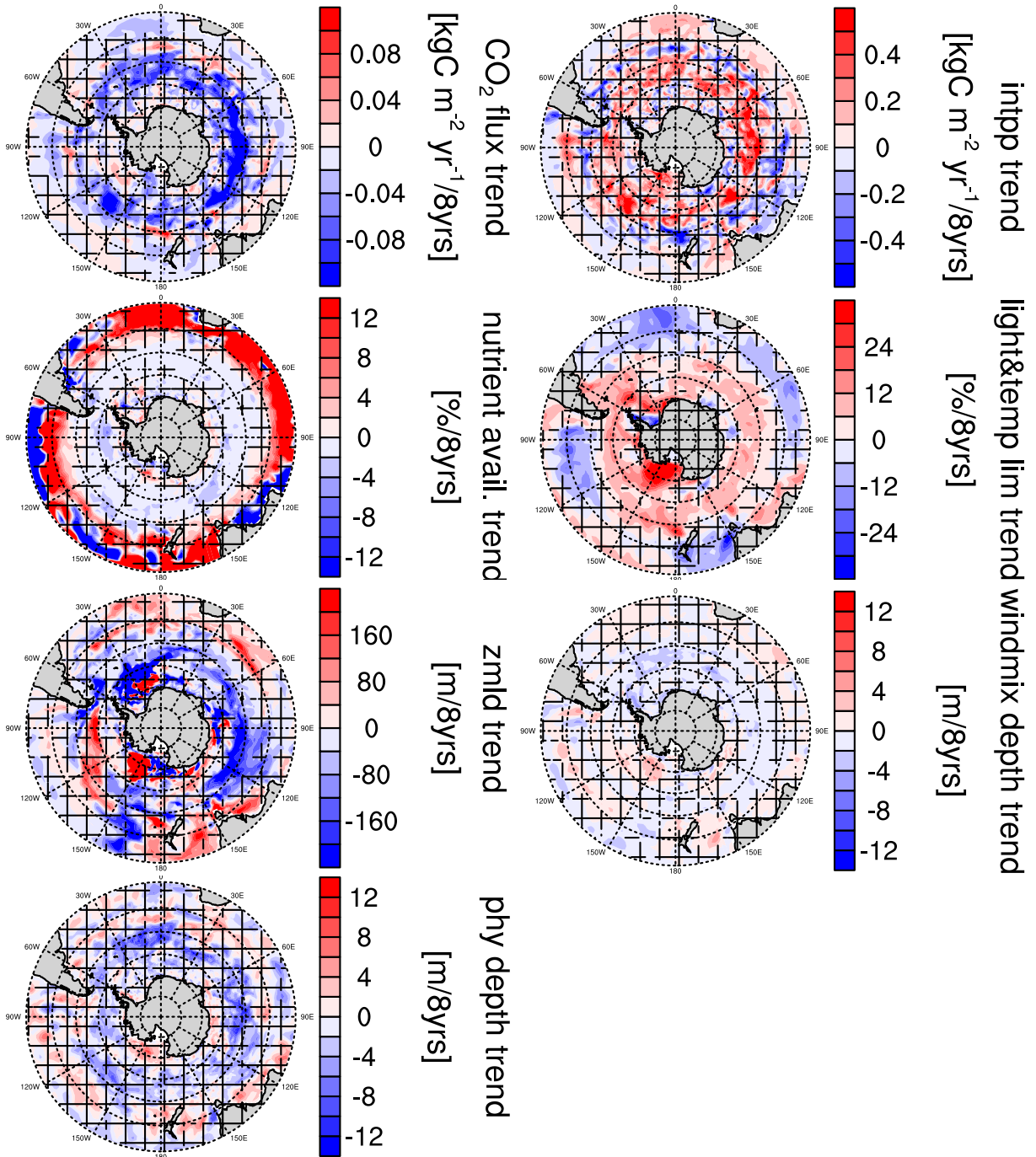


Figure 22: Southern Ocean austral summer trends for the most negative 8-year CO₂ flux trend: CO₂ flux (a), vertically integrated primary production (b), nutrient availability factor (c), surface temperature & limitation function (d), mixed layer depth (e); average depth of vertical diffusivity due to wind (f) and phytoplankton average depth (g); hatched areas indicate where trends are outside the 5% significance level

5 Distinction of drivers in pCO₂

Purpose of pCO₂ separation The previous analysis of thermal, physical and biological controls of the Southern Ocean carbon sink asks for an estimate on the relative contributions of change. As the interconnected processes always influence and change each other directly, a clear and clean separation cannot be taken in precision, but rather for an *estimate of the first-order drivers* in CO₂ flux. In this chapter, I adapt the pCO₂ diagnostics framework from Lovenduski et al. [2007] to quantitatively relate the different contributors to pCO_{2,ocean} and hence CO₂ flux.

5.1 Derivation of the framework

The framework assumes an euphotic zone zonal carbon budget box where at the upper boundary CO₂ enters and at the lower boundary at the mixed-depth layer biology export production leaves the system (fig. 23). Based on the individual processes taking place, a change in pCO₂ due to that process is calculated offline, i.e. from monthly model output data, instead of online, i.e. for each timestep when the model ran.

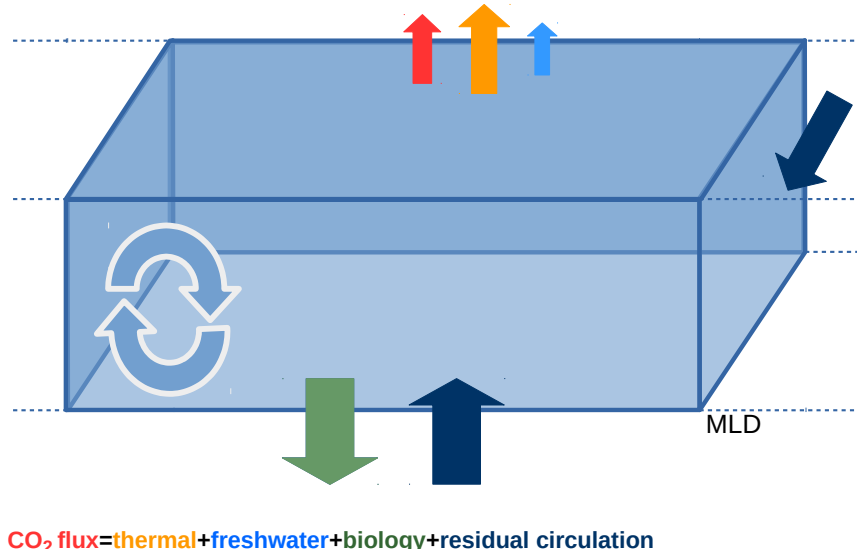


Figure 23: Schematic illustration of pCO₂ driver separation assuming a well-mixed zonal carbon box of the upper-ocean, where CO₂ flux (red) is separated in contributions due to thermal (orange), freshwater (light blue), biology (green) and a residual for circulation (dark blue)

I separate pCO₂ into contributions of temperature, salt, alkalinity and DIC. I use the

salinity-normalized concentrations ($sDIC = \frac{DIC}{S} \cdot (S_0 = 35)$) for DIC and alkalinity to prevent double-accounting of freshwater changes in the DIC/alkalinity and salt contributions [Keeling et al., 2004].

$$\begin{aligned}\delta pCO_2 &= \delta pCO_{2,\text{thermal}} + \delta pCO_{2,\text{salt}} + \delta pCO_{2,\text{alk}} + \delta pCO_{2,\text{DIC}} \\ &= \frac{\partial pCO_2}{\partial T} \delta T + \frac{\partial pCO_2}{\partial S} \delta S + \frac{S}{S_0} \frac{\partial pCO_2}{\partial Alk} \delta sAlk + \frac{S}{S_0} \frac{\partial pCO_2}{\partial DIC} \delta sDIC\end{aligned}$$

The thermal separation is taken from Takahashi et al. [1993]:

$$\frac{\partial pCO_2}{\partial T} \approx pCO_2 \cdot 0.0423^{\circ}C^{-1}.$$

The salinity, DIC and alkalinity contributions are taken from Sarmiento and Gruber [2006]:

$$\begin{aligned}\frac{\partial pCO_2}{\partial S} &\approx \frac{pCO_2}{S} \\ \frac{\partial pCO_2}{\partial DIC} &\approx \frac{pCO_2}{DIC} \cdot \gamma_{DIC} \\ \frac{\partial pCO_2}{\partial Alk} &\approx \frac{pCO_2}{Alk} \cdot \gamma_{Alk} \\ \gamma_{DIC} &\approx \frac{3 \cdot Alk \cdot DIC - 2 \cdot DIC^2}{(2 \cdot DIC - Alk)(Alk - DIC)} \\ \gamma_{Alk} &\approx -\frac{Alk^2}{(2 \cdot DIC - Alk)(Alk - DIC)}.\end{aligned}$$

Furthermore the changes in sDIC and sAlk are separated into biological, air-sea exchange or residual contribution:

$$\frac{\delta(sDIC)}{\delta t} = \frac{\delta(sDIC_{bio})}{\delta t} + \frac{\delta(sDIC_{exchange})}{\delta t} + \frac{\delta(sDIC_{residual})}{\delta t}.$$

The changes due to air-sea exchange and due to biology are converted to DIC and alkalinity changes by dividing by the mixed-layer depth (MLD) assuming a well-mixed mixed-layer depth. Furthermore, the effect of biological primary production contributes with organic matter production and calcium carbonate production to the sDIC changes and calcium carbonate alone accounts for changes in alkalinity.

$$\begin{aligned}sDIC_{bio} &= \frac{coex + caex}{MLD} \\ sDIC_{ex} &= \frac{CO_2flux}{MLD} \\ sAlk_{bio} &= \frac{caex}{MLD}\end{aligned}$$

This approach is based on the following assumptions:

- negligible error in approximations used during derivation
- linearizations of non-linear processes
- simplifications of buffering constants [[Sarmiento and Gruber, 2006](#)]
- residual as combined contribution of [everything which is not described], mainly vertical and lateral circulation, but also to a lesser degree advection of biological constituents
- no problem with monthly mean offline instead of instantaneous online values
- well-mixed mixed layer

5.2 Estimate of pCO₂ drivers

Applying the above described framework yields an estimate for the drivers of pCO₂ for the two extreme trends (table 1).

In general, the trends reverse for opposite wind forcing and the area 50–60°S sets the trend of the overall Southern Ocean carbon sink south of 35°S. The changes in pCO₂ due to biology and temperature are much smaller than the residual circulation change. Biology seems more susceptible to wind-driven changes at 50–60°S than 40–50°S, this separation might be biased by the selection of the latitudinal boundaries.

In detail, the ongoing processes do not simply reverse as the atmospheric forcing trend stays the same. The most positive CO₂ flux trend is mainly driven by the non-thermal pCO_{2,ocean} ocean changes, whereas the most negative CO₂ flux trend is mainly driven by the increasing pCO_{2,atm} concentrations, when the oceanic pCO_{2,ocean} only has a very weak uptake trend.

In the negative CO₂ flux trend, pCO_{2,ocean} due to circulation increases at 40–50°S, whereas less Ekman transport would predict a decrease. Here for the northward shift of the westerlies, the upwelling cell migrated northwards and thus increased the entrainment of carbon-rich waters. Also the warming extends further north into the area of 40–50°S, which shifts the increasing pCO_{2,ocean} trend from cooling out of 40–50°S, resulting in a positive thermal trend.

8-yr trend pCO _{2,x} [ppm]	50–60°S		40–50°S	
	positive	negative	positive	negative
pCO _{2,salt}	0.6	-0.5	0.2	-0.3
pCO _{2,bi} o	2.4	-3.0	-0.7	-0.2
pCO _{2,ex}	-4.8	4.8	0.2	1.1
pCO _{2,circ}	49.2	-9.4	12.3	12.7
pCO _{2,circ,alk}	-2.2	5.5	-3.8	3.7
pCO _{2,non-thermal}	38.2	-8.3	3.4	12.0
pCO _{2,thermal}	-7.1	7.0	6.4	0.5
pCO _{2,ocean}	32.2	-2.4	9.4	12.9
pCO _{2,atm}	12.0	14.5	12.0	14.5
dpCO ₂	20.2	-16.9	-2.6	-1.6

Table 1: Trends in drivers of pCO₂ for the most extreme positive CO₂ flux trend and the most most extreme negative CO₂ flux trend

positive CO₂ flux trend Now, I combine these three distinct CO₂ flux responses into a comprehensive picture (fig. 24). While the cooling effect of the stronger winds reduces outgassing in the high-latitude Southern Ocean, the increase in upwelling of carbon-rich

waters and the decline in primary production outplay the thermal effect to a relative outgassing trend at 50-60°S. At 40-50°S the warming effect and increased Ekman transport DIC supply reduces carbon uptake, which is overtrumped by increase primary production and increased downwelling and leads to a combined relative CO₂ uptake trend. The resulting CO₂ flux signal at 50-60°S is stronger than the one at 40-50°S and hence determines the overall Southern Ocean carbon sink trend. The overall positive CO₂ flux trend and its opposite thermal contribution is inline with Lovenduski et al. [2007].

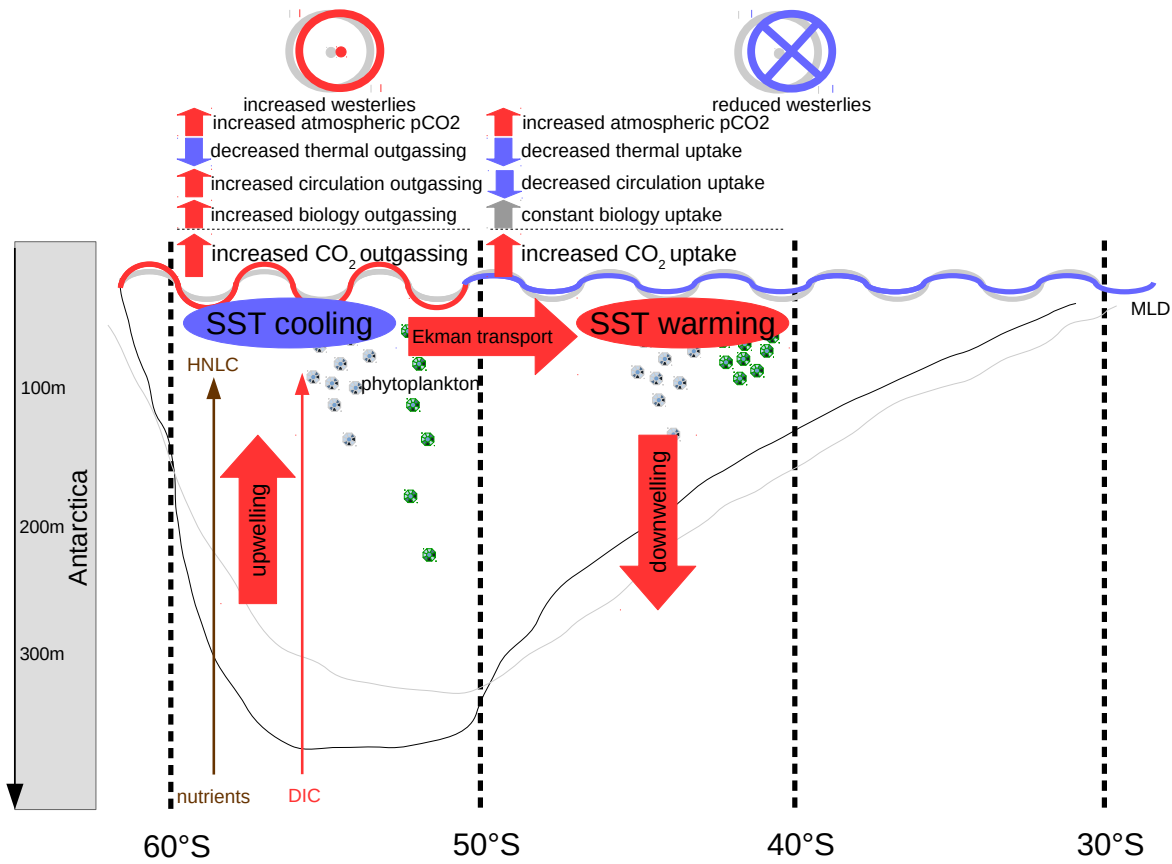


Figure 24: Schematic illustration of the Southern Ocean under the context of increasing westerly winds and response in the thermal effect, biology and upper-ocean circulation leading towards a positive CO₂ flux trend; red color-coding indicates a relative increase of the related quantity or process whereas blue indicates a relative decrease. Stronger winds enhance the upper-ocean overturning circulation. Increased upwelling increases outgassing of over-saturated carbon-rich deep waters. Increased Ekman transport advects DIC further north, cools the higher latitudes whereas it warms the lower latitudes. Deeper mixing and cooling in the higher latitudes decreases primary production whereas shallower mixing and warming increase primary production in the higher latitudes.

negative CO₂ flux trend The three distinct CO₂ flux responses from chapter 4.3 merge into the opposing picture as for decreasing westerly winds (fig. 25). While the warming effect of the weaker winds increases outgassing in the high-latitude Southern Ocean, the decrease in upwelling of carbon-rich waters and the decline in primary production outplay the thermal effect to a relative ingassing trend at 50-60°S. At 40-50°S the cooling effect and decreased Ekman transport DIC supply relatively increase carbon uptake, which is overtrumped by decreased primary production and decreased downwelling and leads to a combined relative CO₂ outgassing trend. The resulting CO₂ flux signal at 50-60°S is stronger than the one at 40-50°S and hence determines the overall Southern Ocean carbon sink trend.

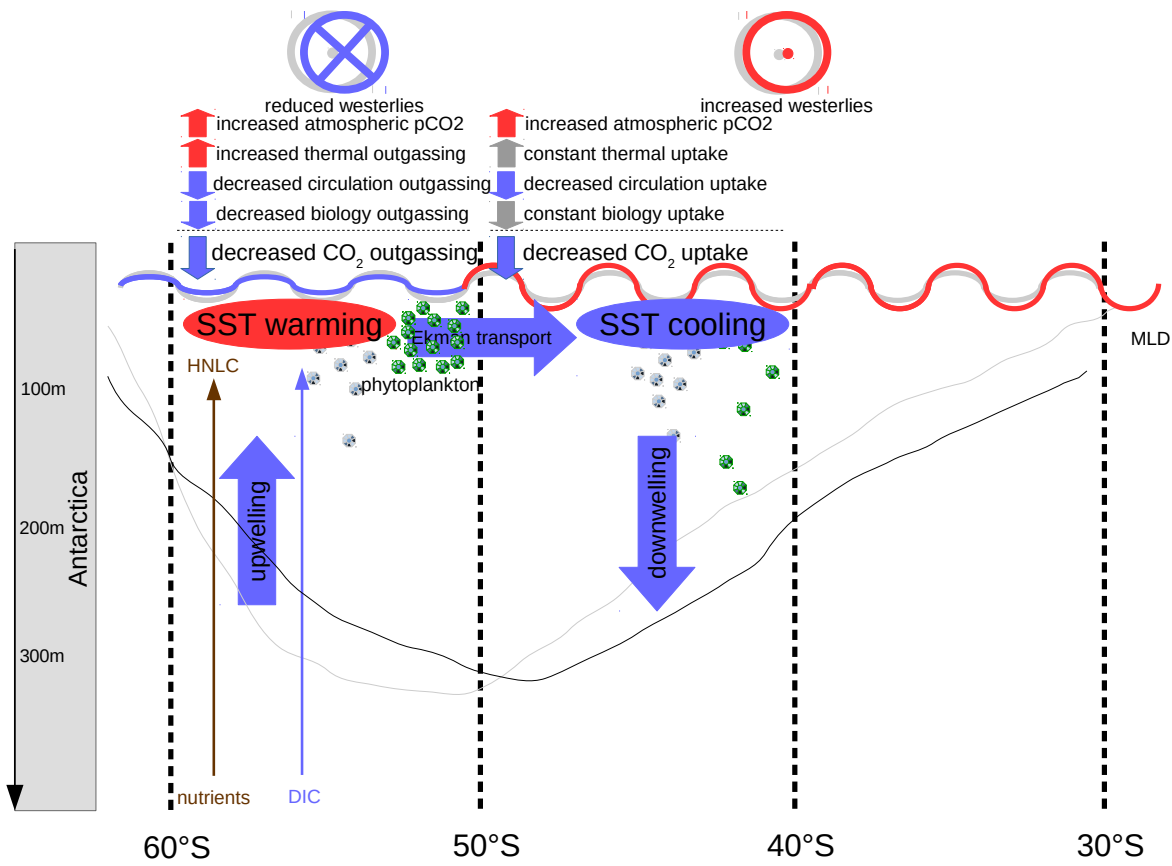


Figure 25: Schematic illustration of the Southern Ocean under the context of decreasing westerly winds and response in the thermal effect, biology and upper-ocean circulation leading towards a negative CO₂ flux trend; red color-coding indicates a relative increase of the related quantity or process, whereas blue indicates a relative decrease. Stronger winds decrease the upper-ocean overturning circulation. Decreased upwelling lowers outgassing of over-saturated carbon-rich deep waters. Decreased Ekman transport advects less DIC to the north, warms the higher latitudes whereas it cools the lower latitudes. Shallower mixing and warming in the higher latitudes increases primary production, whereas deeper mixing and cooling decrease primary production in the higher latitudes.

6 Summary and conclusions

what I did and internal variability value $\pm X$; make sure research questions are answered Analyzing 100 historical MPI-ESM simulations in the historical period for which the observational CO₂ flux product SOM-FFN is available, I estimate the modeled decadal internal variability $\sigma_{DIV} \approx 0.18 \text{ PgC/yr}$ (see fig. 4). The area of largest decadal variability is at 50-60°S (see fig. 3b). MPI-ESM LE contains decades with CO₂ flux trend of similar magnitude and monotony as suggested by observations [Landschützer et al., 2015] (see fig. A.2). The variability in strength and position of westerly winds dominates the variability in CO₂ flux with two distinct wind-driven regimes (see fig. 12): Stronger and southward shifting westerly winds associated with a positive trend in the Southern Annular Mode reduce the Southern Ocean carbon sink by enhanced outgassing of carbon-rich deep waters against the atmospheric increase of pCO_{2,atm}. This outgassing is reduced for weakening and northward shifted westerly winds and leads to an increase in the Southern Ocean carbon sink supported by the atmospheric increase of pCO_{2,atm}. [how deep should the summary of processes go? now its shallow! should I talk about thermal, bio and circulation explicitly - I already summarize processes in the chapter before]

Comparability to observations What do we learn from this large ensemble simulation for the Southern Ocean carbon sink? MPI-ESM LE does not aim to reproduce CO₂ flux trends suggested by observations, but it proves perturbed initial conditions large ensemble simulations are capable of capturing decadal internal variations similar to observations; even if this only applies for the most extreme decadal trends.

Comparing quantitatively, the modeled internal variability without prescribed pCO_{2,atm} but historical CO₂ emissions would increase by 25%, when the oceanic and terrestrial carbon sink are connected [Ilyina et al., 2013].

A flaw for comparability is the parametrization of eddies in MPI-ESM. The increasing trend of winds have mixing effect on seasonal scale, but for longer periods eddies would weaken those trends [Thompson et al., 2011]. This might reduce the deeper mixing in multi-year trends and asks for high-resolution perturbed initial conditions large ensemble simulations. [IMPLICATIONS? lets discuss]

Outlook: large ensemble variability modeling The history of perturbed large initial conditions simulation is fairly recent. The attempt to study internal variability with MPI-ESM Large Ensemble shows the insight into internal variability with many realizations and is important to understand internal varying processes in our climate system. These processes might become increasingly important in the case of global CO₂ emission reductions, when the CO₂ reduction efforts are tracked by new measurements and evaluated by politicians and scientists [Hawkins and Sutton, 2009, Lovenduski et al., 2015, Marotzke et al., 2017]. A further interesting project would be the comparison of different perturbed initial conditions large ensembles based on different models.

Outlook: observational focus on Southern Ocean For the Southern Ocean, however, there is a desperate need for increase amount of measurements to understand the Southern Ocean and its biogeochemical properties. The recent ARGO data and the newly deployed biogeochemical floats currently advance the basis for understanding in the Southern Ocean.

References and Notes

- R. Abernathey, J. Marshall, and D. Ferreira. The dependence of southern ocean meridional overturning on wind stress. *J. Phys. Oceanogr.*, 41(12):2261–2278, dec 2011. doi: 10.1175/jpo-d-11-023.1. URL <http://dx.doi.org/10.1175/JPO-D-11-023.1>.
- D. C. E. Bakker, B. Pfeil, K. Smith, S. Hankin, A. Olsen, S. R. Alin, C. Cosca, S. Harasawa, A. Kozyr, Y. Nojiri, K. M. O'Brien, U. Schuster, M. Telszewski, B. Tilbrook, C. Wada, J. Akl, L. Barbero, N. R. Bates, J. Boutin, Y. Bozec, W.-J. Cai, R. D. Castle, F. P. Chavez, L. Chen, M. Chierici, K. Currie, H. J. W. de Baar, W. Evans, R. A. Feely, A. Fransson, Z. Gao, B. Hales, N. J. Hardman-Mountford, M. Hoppema, W.-J. Huang, C. W. Hunt, B. Huss, T. Ichikawa, T. Johannessen, E. M. Jones, S. D. Jones, S. Jutterstrm, V. Kitidis, A. Krtzinger, P. Landschtzer, S. K. Lauvset, N. Lefevre, A. B. Manke, J. T. Mathis, L. Merlivat, N. Metzl, A. Murata, T. Newberger, A. M. Omar, T. Ono, G.-H. Park, K. Paterson, D. Pierrot, A. F. Ríos, C. L. Sabine, S. Saito, J. Salisbury, V. V. S. S. Sarma, R. Schlitzer, R. Sieger, I. Skjelvan, T. Steinhoff, K. F. Sullivan, H. Sun, A. J. Sutton, T. Suzuki, C. Sweeney, T. Takahashi, J. Tjiputra, N. Tsurushima, S. M. A. C. van Heuven, D. Vandemark, P. Vlahos, D. W. R. Wallace, R. Wanninkhof, and A. J. Watson. An update to the surface ocean CO₂ atlas (SOCAT version 2). *Earth System Science Data*, 6(1):69–90, mar 2014. doi: 10.5194/essd-6-69-2014. URL <https://doi.org/10.5194%2Fessd-6-69-2014>.
- M. J. Behrenfeld. Climate-mediated dance of the plankton. *Nature Climate Change*, 4 (10):880–887, sep 2014. doi: 10.1038/nclimate2349. URL <https://doi.org/10.1038%2Fnclimate2349>.
- M. Bittner, H. Schmidt, C. Timmreck, and F. Sienz. Using a large ensemble of simulations to assess the Northern Hemisphere stratospheric dynamical response to tropical volcanic eruptions and its uncertainty. *Geophysical Research Letters*, 43(17):9324–9332, 2016. ISSN 1944-8007. doi: 10.1002/2016GL070587. URL <http://dx.doi.org/10.1002/2016GL070587>. 2016GL070587.
- L. Bopp, L. Resplandy, J. C. Orr, S. C. Doney, J. P. Dunne, M. Gehlen, P. Halloran, C. Heinze, T. Ilyina, R. Séférian, J. Tjiputra, and M. Vichi. Multiple stressors of ocean ecosystems in the 21st century: projections with CMIP5 models. *Biogeosciences*, 10

(10):6225–6245, oct 2013. doi: 10.5194/bg-10-6225-2013. URL <https://doi.org/10.5194%2Fbg-10-6225-2013>.

C. Deser, A. Phillips, V. Bourdette, and H. Teng. Uncertainty in climate change projections: the role of internal variability. *Clim Dyn*, 38(3-4):527–546, dec 2012. doi: 10.1007/s00382-010-0977-x. URL <http://dx.doi.org/10.1007/s00382-010-0977-x>.

T. DeVries, M. Holzer, and F. Primeau. Recent increase in oceanic carbon uptake driven by weaker upper-ocean overturning. *Nature*, 542(7640):215–218, feb 2017. doi: 10.1038/nature21068. URL <https://doi.org/10.1038%2Fnature21068>.

K. Döös and D. J. Webb. The deacon cell and the other meridional cells of the southern ocean. *Journal of Physical Oceanography*, 24(2):429–442, 1994. doi: 10.1175/1520-0485(1994)024<0429:TDCATO>2.0.CO;2. URL [http://dx.doi.org/10.1175/1520-0485\(1994\)024<0429:TDCATO>2.0.CO;2](http://dx.doi.org/10.1175/1520-0485(1994)024<0429:TDCATO>2.0.CO;2).

C. O. Dufour, J. L. Sommer, M. Gehlen, J. C. Orr, J.-M. Molines, J. Simeon, and B. Barnier. Eddy compensation and controls of the enhanced sea-to-air CO₂ flux during positive phases of the southern annular mode. *Global Biogeochemical Cycles*, 27(3):950–961, sep 2013. doi: 10.1002/gbc.20090. URL <http://dx.doi.org/10.1002/gbc.20090>.

R. W. Eppley. Temperature and phytoplankton growth in the sea. *Fishery Bulletin*, 70(4):1063–1085, 1972.

B. Falkowski, P. G., R. T., and V. Smetacek. Biogeochemical controls and feedbacks on and ocean primary production. *Science*, 281(5374):200–206, 1998. doi: 10.1126/science.281.5374.200. URL <http://science.sciencemag.org/content/281/5374/200>.

P. J. S. Franks. Has sverdrup’s critical depth hypothesis been tested? mixed layers vs. turbulent layers. *ICES Journal of Marine Science: Journal du Conseil*, 72(6):1897–1907, oct 2014. doi: 10.1093/icesjms/fsu175.

H. E. Garcia, R. A. Locarnini, T. P. Boyer, J. I. Antonov, O. Baranova, M. Zweng, J. Reagan, and D. Johnson. *World Ocean Atlas 2013, Volume 4: Dissolved Inorganic*

- Nutrients (phosphate, nitrate, silicate)*, volume 76 of 25. NOAA Atlas NESDIS, 2013.
URL <https://www.nodc.noaa.gov/OC5/woa13/pubwoa13.html>.
- P. R. Gent, J. Willebrand, T. J. McDougall, and J. C. McWilliams. Parameterizing eddy-induced tracer transports in ocean circulation models. *Journal of Physical Oceanography*, 25(4):463–474, 1995. doi: 10.1175/1520-0485(1995)025<0463:PEITTI>2.0.CO;2. URL [http://dx.doi.org/10.1175/1520-0485\(1995\)025<0463:PEITTI>2.0.CO;2](http://dx.doi.org/10.1175/1520-0485(1995)025<0463:PEITTI>2.0.CO;2).
- R. O. Gilbert. *Statistical Methods for Environmental Pollution Monitoring*. Wiley, 1987.
- M. A. Giorgetta, J. Jungclaus, C. H. Reick, S. Legutke, J. Bader, M. Böttinger, V. Brovkin, T. Crueger, M. Esch, K. Fieg, K. Glushak, V. Gayler, H. Haak, H.-D. Hollweg, T. Ilyina, S. Kinne, L. Kornblueh, D. Matei, T. Mauritsen, U. Mikolajewicz, W. Mueller, D. Notz, F. Pithan, T. Raddatz, S. Rast, R. Redler, E. Roeckner, H. Schmidt, R. Schnur, J. Segschneider, K. D. Six, M. Stockhausen, C. Timmreck, J. Wegner, H. Widmann, K.-H. Wieners, M. Claussen, J. Marotzke, and B. Stevens. Climate and carbon cycle changes from 1850 to 2100 in mpi-esm simulations for the coupled model intercomparison project phase 5. *Journal of Advances in Modeling Earth Systems*, 5(3):572–597, 2013. ISSN 1942-2466. doi: 10.1002/jame.20038. URL <http://dx.doi.org/10.1002/jame.20038>.
- A. Gnanadesikan, M.-A. Pradal, and R. Abernathey. Isopycnal mixing by mesoscale eddies significantly impacts oceanic anthropogenic carbon uptake. *Geophysical Research Letters*, 42(11):4249–4255, jun 2015. doi: 10.1002/2015gl064100. URL <https://doi.org/10.1002%2F2015gl064100>.
- D. Gong and S. Wang. Definition of Antarctic Oscillation index. *Geophysical Research Letters*, 26(4):459–462, 1999. ISSN 1944-8007. doi: 10.1029/1999GL900003. URL <http://dx.doi.org/10.1029/1999GL900003>.
- A. Hall and M. Visbeck. Synchronous Variability in the Southern Hemisphere Atmosphere, Sea Ice, and Ocean Resulting from the Annular Mode. *Journal of Climate*, 15(21):3043–3057, 2002. doi: 10.1175/1520-0442(2002)015<3043:SVITSH>2.0.CO;2. URL [http://dx.doi.org/10.1175/1520-0442\(2002\)015<3043:SVITSH>2.0.CO;2](http://dx.doi.org/10.1175/1520-0442(2002)015<3043:SVITSH>2.0.CO;2).
- J. Hauck, C. Völker, T. Wang, M. Hoppema, M. Losch, and D. A. Wolf-Gladrow. Seasonally different carbon flux changes in the southern ocean in response to the south-

- ern annular mode. *Global Biogeochemical Cycles*, 27(4):1236–1245, dec 2013. doi: 10.1002/2013gb004600. URL <http://dx.doi.org/10.1002/2013GB004600>.
- F. A. Haumann, D. Notz, and H. Schmidt. Anthropogenic influence on recent circulation-driven antarctic sea ice changes. *Geophysical Research Letters*, 41(23):8429–8437, dec 2014. doi: 10.1002/2014gl061659. URL <https://doi.org/10.1002%2F2014gl061659>.
- E. Hawkins and R. Sutton. The Potential to Narrow Uncertainty in Regional Climate Predictions. *Bulletin of the American Meteorological Society*, 90(8):1095–1107, 2009. doi: 10.1175/2009BAMS2607.1. URL <http://dx.doi.org/10.1175/2009BAMS2607.1>.
- C. Heinze, E. Maier-Reimer, A. M. E. Winguth, and D. Archer. A global oceanic sediment model for long-term climate studies. *Global Biogeochemical Cycles*, 13(1):221–250, 1999. ISSN 1944-9224. doi: 10.1029/98GB02812. URL <http://dx.doi.org/10.1029/98GB02812>.
- C. Heuzé, K. J. Heywood, D. P. Stevens, and J. K. Ridley. Southern ocean bottom water characteristics in CMIP5 models. *Geophys. Res. Lett.*, 40(7):1409–1414, apr 2013. doi: 10.1002/grl.50287. URL <http://dx.doi.org/10.1002/grl.50287>.
- R. Hirsch, J. Slack, and R. Smith. Techniques of trend analysis for monthly water quality data. *Water Resources Research*, 18(1):107–121, 1982.
- T. Ilyina. Hidden trends in the ocean carbon sink. *Nature*, 530(7591):426–427, February 2016. doi: 10.1038/530426a. URL <http://www.nature.com/nature/journal/v530/n7591/pdf/530426a.pdf>.
- T. Ilyina, K. D. Six, J. Segschneider, E. Maier-Reimer, H. Li, and I. Núñez-Riboni. Global ocean biogeochemistry model hamocc: Model architecture and performance as component of the mpi-earth system model in different cmip5 experimental realizations. *Journal of Advances in Modeling Earth Systems*, 5(2):287–315, 2013. ISSN 1942-2466. doi: 10.1029/2012MS000178. URL <http://dx.doi.org/10.1029/2012MS000178>.
- IPCC. *Climate Change 2013: The Physical Science Basis. Contribution of Working Group I to the Fifth Assessment Report on the Intergovernmental Panel on Climate Change*. Cambridge University Press, 2013.

- J. H. Jungclaus, N. Fischer, H. Haak, K. Lohmann, J. Marotzke, D. Matei, U. Mikolajewicz, D. Notz, and J. S. von Storch. Characteristics of the ocean simulations in the max planck institute ocean model (mpiom) the ocean component of the mpi-earth system model. *Journal of Advances in Modeling Earth Systems*, 5(2):422–446, 2013. ISSN 1942-2466. doi: 10.1002/jame.20023. URL <http://dx.doi.org/10.1002/jame.20023>.
- E. Kalnay, M. Kanamitsu, R. Kistler, W. Collins, D. Deaven, L. Gandin, M. Iredell, S. Saha, G. White, J. Woollen, Y. Zhu, A. Leetmaa, R. Reynolds, M. Chelliah, W. Ebisuzaki, W. Higgins, J. Janowiak, K. C. Mo, C. Ropelewski, J. Wang, R. Jenne, and D. Joseph. The NCEP/NCAR 40-Year Reanalysis Project. *Bulletin of the American Meteorological Society*, 77(3):437471, 1996. doi: 10.1175/1520-0477(1996)077<0437:TNYRP>2.0.CO;2. URL [http://dx.doi.org/10.1175/1520-0477\(1996\)077<0437:TNYRP>2.0.CO;2](http://dx.doi.org/10.1175/1520-0477(1996)077<0437:TNYRP>2.0.CO;2).
- J. E. Kay, C. Deser, A. Phillips, A. Mai, C. Hannay, G. Strand, J. M. Arblaster, S. C. Bates, G. Danabasoglu, J. Edwards, M. Holland, P. Kushner, J.-F. Lamarque, D. Lawrence, K. Lindsay, A. Middleton, E. Munoz, R. Neale, K. Oleson, L. Polvani, and M. Vertenstein. The community earth system model (CESM) large ensemble project: A community resource for studying climate change in the presence of internal climate variability. *Bull. Amer. Meteor. Soc.*, 96(8):1333–1349, aug 2015. doi: 10.1175/bams-d-13-00255.1. URL <http://dx.doi.org/10.1175/BAMS-D-13-00255.1>.
- C. D. Keeling, H. Brix, and N. Gruber. Seasonal and long-term dynamics of the upper ocean carbon cycle at station aloha near hawaii. *Global Biogeochemical Cycles*, 18(4):n/a–n/a, 2004. ISSN 1944-9224. doi: 10.1029/2004GB002227. URL <http://dx.doi.org/10.1029/2004GB002227>. GB4006.
- M. G. Kendall. *Rank Correlation Methods*. Charles Griffin, 1975.
- A. Kessler and J. Tjiputra. The southern ocean as a constraint to reduce uncertainty in future ocean carbon sinks. *Earth Syst. Dynam.*, 7(2):295–312, apr 2016. doi: 10.5194/esd-7-295-2016. URL <http://dx.doi.org/10.5194/esd-7-295-2016>.
- J. Kidston and E. P. Gerber. Intermodel variability of the poleward shift of the austral jet stream in the CMIP3 integrations linked to biases in 20th century climatology.

Geophysical Research Letters, 37(9):n/a–n/a, 2010. ISSN 1944-8007. doi: 10.1029/2010GL042873. URL <http://dx.doi.org/10.1029/2010GL042873>. L09708.

K. M. Krumhardt, N. S. Lovenduski, M. C. Long, and K. Lindsay. Avoidable impacts of ocean warming on marine primary production: Insights from the CESM ensembles. *Global Biogeochemical Cycles*, 31(1):114–133, jan 2017. doi: 10.1002/2016gb005528. URL <https://doi.org/10.1002%2F2016gb005528>.

P. Landschützer, N. Gruber, D. C. E. Bakker, and U. Schuster. Recent variability of the global ocean carbon sink. *Global Biogeochemical Cycles*, 28(9):927–949, sep 2014. doi: 10.1002/2014gb004853. URL <http://dx.doi.org/10.1002/2014GB004853>.

P. Landschützer, N. Gruber, F. A. Haumann, C. Rödenbeck, D. C. E. Bakker, S. van Heuven, M. Hoppema, N. Metzl, C. Sweeney, T. Takahashi, B. Tilbrook, and R. Wanninkhof. The reinvigoration of the southern ocean carbon sink. *Science*, 349(6253):1221–1224, 2015. ISSN 0036-8075. doi: 10.1126/science.aab2620. URL <http://science.sciencemag.org/content/349/6253/1221>.

J. M. Lauderdale, A. C. N. Garabato, K. I. C. Oliver, M. J. Follows, and R. G. Williams. Wind-driven changes in southern ocean residual circulation, ocean carbon reservoirs and atmospheric co₂. *Climate Dynamics*, 41(7):2145–2164, 2013. ISSN 1432-0894. doi: 10.1007/s00382-012-1650-3. URL <http://dx.doi.org/10.1007/s00382-012-1650-3>.

J. M. Lauderdale, R. G. Williams, D. R. Munday, and D. P. Marshall. The impact of southern ocean residual upwelling on atmospheric CO₂ on centennial and millennial timescales. *Clim Dyn*, may 2016. doi: 10.1007/s00382-016-3163-y. URL <http://dx.doi.org/10.1007/s00382-016-3163-y>.

C. Le Quéré, C. Rödenbeck, E. T. Buitenhuis, T. J. Conway, R. Langenfelds, A. Gomez, C. Labuschagne, M. Ramonet, T. Nakazawa, N. Metzl, N. Gillett, and M. Heimann. Saturation of the southern ocean co₂ sink due to recent climate change. *Science*, 316(5832):1735–1738, 2007. ISSN 0036-8075. doi: 10.1126/science.1136188. URL <http://science.sciencemag.org/content/316/5832/1735>.

C. Le Quéré, E. T. Buitenhuis, R. Moriarty, S. Alvain, O. Aumont, L. Bopp, S. Chollet, C. Enright, D. J. Franklin, R. J. Geider, S. P. Harrison, A. G. Hirst, S. Larsen,

- L. Legendre, T. Platt, I. C. Prentice, R. B. Rivkin, S. Sailley, S. Sathyendranath, N. Stephens, M. Vogt, and S. M. Vallina. Role of zooplankton dynamics for southern ocean phytoplankton biomass and global biogeochemical cycles. *Biogeosciences*, 13(14):4111–4133, jul 2016. doi: 10.5194/bg-13-4111-2016. URL <http://dx.doi.org/10.5194/bg-13-4111-2016>.
- N. S. Lovenduski and N. Gruber. Impact of the southern annular mode on southern ocean circulation and biology. *Geophys. Res. Lett.*, 32(L11603), 2005. doi: 10.1029/2005GL022727. URL <http://onlinelibrary.wiley.com/doi/10.1029/2005GL022727/pdf>.
- N. S. Lovenduski, N. Gruber, S. C. Doney, and I. D. Lima. Enhanced CO_2 outgassing in the southern ocean from a positive phase of the southern annular mode. *Global Biogeochemical Cycles*, 21(2), 2007. ISSN 1944-9224. doi: 10.1029/2006GB002900. URL <http://dx.doi.org/10.1029/2006GB002900>. GB2026.
- N. S. Lovenduski, N. Gruber, and S. C. Doney. Toward a mechanistic understanding of the decadal trends in the southern ocean carbon sink. *Global Biogeochem. Cycles*, 22, 2008. doi: 10.1029/2007GB003139.
- N. S. Lovenduski, A. R. Fay, and G. A. McKinley. Observing multidecadal trends in southern ocean CO_2 uptake: What can we learn from an ocean model? *Global Biogeochem. Cycles*, 29(4):416–426, apr 2015. doi: 10.1002/2014gb004933. URL <http://dx.doi.org/10.1002/2014GB004933>.
- N. S. Lovenduski, G. A. McKinley, A. R. Fay, K. Lindsay, and M. C. Long. Partitioning uncertainty in ocean carbon uptake projections: Internal variability, emission scenario, and model structure. *Global Biogeochemical Cycles*, 30(9):1276–1287, sep 2016. doi: 10.1002/2016gb005426. URL <http://dx.doi.org/10.1002/2016GB005426>.
- M. S. Lozier, A. C. Dave, J. B. Palter, L. M. Gerber, and R. T. Barber. On the relationship between stratification and primary productivity in the North Atlantic. *Geophysical Research Letters*, 38(18):n/a–n/a, 2011. ISSN 1944-8007. doi: 10.1029/2011GL049414. URL <http://dx.doi.org/10.1029/2011GL049414>. L18609.
- E. Maier-Reimer. Toward a global ocean carbon model. *Progress in Biometeorology*, 3: 295–310, 1984.

- E. Maier-Reimer. Geochemical cycles in an ocean general circulation model. preindustrial tracer distributions. *Global Biogeochem. Cycles*, 7(3):645–677, September 1993.
- H. B. Mann. Non-parametric tests against trend. *Econometrica*, 13:163–171, 1945.
- J. Marotzke, C. Jakob, S. Bony, P. A. Dirmeyer, P. A. O’Gorman, E. Hawkins, S. Perkins-Kirkpatrick, C. L. Quéré, S. Nowicki, K. Paulavets, S. I. Seneviratne, B. Stevens, and M. Tuma. Climate research must sharpen its view. *Nature Climate Change*, 7:89–91, 2017.
- G. J. Marshall. Trends in the southern annular mode from observations and reanalyses. *Journal of Climate*, 16(24):4134–4143, 2003. doi: 10.1175/1520-0442(2003)016<4134:TTSAM>2.0.CO;2. URL <https://legacy.bas.ac.uk/met/gjma/sam.html>.
- S. Marsland, H. Haak, J. Jungclaus, M. Latif, and F. Röske. The max-planck-institute global ocean/sea ice model with orthogonal curvilinear coordinates. *Ocean Modelling*, 5(2):91 – 127, 2003. ISSN 1463-5003. doi: [http://dx.doi.org/10.1016/S1463-5003\(02\)00015-X](http://dx.doi.org/10.1016/S1463-5003(02)00015-X). URL <http://www.sciencedirect.com/science/article/pii/S146350030200015X>.
- J. H. Martin. Glacial-interglacial CO₂ change: The Iron Hypothesis. *Paleoceanography*, 5(1):1–13, 1990. ISSN 1944-9186. doi: 10.1029/PA005i001p00001. URL <http://dx.doi.org/10.1029/PA005i001p00001>.
- J. H. Martin, R. M. Gordon, and S. E. Fitzwater. Iron in antarctic waters. *Nature*, 345: 156–158, 1990. doi: 10.1038/345156a0.
- G. A. McKinley, D. J. Pilcher, A. R. Fay, K. Lindsay, M. C. Long, and N. S. Lovenduski. Timescales for detection of trends in the ocean carbon sink. *Nature*, 530(7591): 469–472, feb 2016. doi: 10.1038/nature16958. URL <http://dx.doi.org/10.1038/nature16958>.
- L. Michaelis and M. L. Menten. Die kinetik der invertinwirkung. *Biochem. Z.*, 49:333–369, 1913.
- G. Monterey and S. Levitus. Seasonal variability of the mixed layer depth for the world ocean. resreport, NOAA Atlas NESDIS 14, 1997.

- A. M. Mood, F. A. Graybill, and D. C. Boes. *Introduction to the Theory of Statistics*. McGraw-Hill, 1974.
- C. D. Nevison, M. Manizza, R. F. Keeling, B. B. Stephens, J. D. Bent, J. Dunne, T. Ilyina, M. Long, L. Resplandy, J. Tjiputra, and S. Yukimoto. Evaluating CMIP5 ocean biogeochemistry and southern ocean carbon uptake using atmospheric potential oxygen: Present-day performance and future projection. *Geophys. Res. Lett.*, 43(5):2077–2085, mar 2016. doi: 10.1002/2015gl067584. URL <http://dx.doi.org/10.1002/2015GL067584>.
- A. H. Orsi, T. Whitworth, and W. D. Nowlin. On the meridional extent and fronts of the antarctic circumpolar current. *Deep Sea Research Part I: Oceanographic Research Papers*, 42(5):641 – 673, 1995. ISSN 0967-0637. doi: [http://dx.doi.org/10.1016/0967-0637\(95\)00021-W](http://dx.doi.org/10.1016/0967-0637(95)00021-W). URL <http://www.sciencedirect.com/science/article/pii/096706379500021W>.
- R. C. Pacanowski and S. G. H. Philander. Parameterization of Vertical Mixing in Numerical Models of Tropical Oceans. *Journal of Physical Oceanography*, 11(11):1443–1451, 1981. doi: 10.1175/1520-0485(1981)011<1443:POVMIN>2.0.CO;2. URL [http://dx.doi.org/10.1175/1520-0485\(1981\)011<1443:POVMIN>2.0.CO;2](http://dx.doi.org/10.1175/1520-0485(1981)011<1443:POVMIN>2.0.CO;2).
- T. Platt and A. D. Jassby. The relationship between photosynthesis and light for natural assemblages of coastal marine phytoplankton. *Journal of Phycology*, 12(4):421–430, 1976. ISSN 1529-8817. doi: 10.1111/j.1529-8817.1976.tb02866.x. URL <http://dx.doi.org/10.1111/j.1529-8817.1976.tb02866.x>.
- C. H. Reick, T. Raddatz, V. Brovkin, and V. Gayler. Representation of natural and anthropogenic land cover change in MPI-ESM. *Journal of Advances in Modeling Earth Systems*, 5(3):459–482, 2013. ISSN 1942-2466. doi: 10.1002/jame.20022. URL <http://dx.doi.org/10.1002/jame.20022>.
- L. Resplandy, R. Séférian, and L. Bopp. Natural variability of CO₂ and O₂ fluxes: What can we learn from centuries-long climate models simulations? *Journal of Geophysical Research: Oceans*, 120(1):384–404, jan 2015. doi: 10.1002/2014jc010463. URL <https://doi.org/10.1002%2F2014jc010463>.

- C. Rödenbeck, R. F. Keeling, D. C. E. Bakker, N. Metzl, A. Olsen, C. Sabine, and M. Heimann. Global surface-ocean co₂ and sea-air co₂ flux variability from an observation-driven ocean mixed-layer scheme. *Ocean Sci.*, 9(2):193–216, mar 2013. doi: 10.5194/os-9-193-2013. URL <http://dx.doi.org/10.5194/os-9-193-2013>.
- C. Rödenbeck, D. C. E. Bakker, N. Metzl, A. Olsen, C. Sabine, N. Cassar, F. Reum, R. F. Keeling, and M. Heimann. Interannual seaair co₂ flux variability from an observation-driven ocean mixed-layer scheme. *Biogeosciences*, 11(17):4599–4613, 2014. doi: 10.5194/bg-11-4599-2014. URL <http://www.biogeosciences.net/11/4599/2014/>.
- C. Rödenbeck, D. C. E. Bakker, N. Gruber, Y. Iida, A. R. Jacobson, S. Jones, P. Landschützer, N. Metzl, S. Nakaoka, A. Olsen, G.-H. Park, P. Peylin, K. B. Rodgers, T. P. Sasse, U. Schuster, J. D. Shutler, V. Valsala, R. Wanninkhof, and J. Zeng. Data-based estimates of the ocean carbon sink variability – first results of the surface ocean CO₂ mapping intercomparison (SOCOM). *Biogeosciences*, 12(23):7251–7278, dec 2015. doi: 10.5194/bg-12-7251-2015. URL <https://doi.org/10.5194%2Fbg-12-7251-2015>.
- K. B. Rodgers, J. Lin, and T. L. Frlicher. Emergence of multiple ocean ecosystem drivers in a large ensemble suite with an earth system model. *Biogeosciences*, 12(11):3301–3320, jun 2015. doi: 10.5194/bg-12-3301-2015. URL <https://doi.org/10.5194%2Fbg-12-3301-2015>.
- C. L. Sabine, R. A. Feely, N. Gruber, R. M. Key, K. Lee, J. L. Bullister, R. Wanninkhof, C. S. Wong, D. W. R. Wallace, B. Tilbrook, F. J. Millero, T.-H. Peng, A. Kozyr, T. Ono, and A. F. Rios. The oceanic sink for anthropogenic co₂. *Science*, 305(5682):367–371, 2004. ISSN 0036-8075. doi: 10.1126/science.1097403. URL <http://science.sciencemag.org/content/305/5682/367>.
- J. B. Sallée, K. G. Speer, and S. R. Rintoul. Zonally asymmetric response of the southern ocean mixed-layer depth to the southern annular mode. *Nature Geoscience*, 3(4):273–279, mar 2010. doi: 10.1038/ngeo812. URL <http://dx.doi.org/10.1038/NGE0812>.
- J.-B. Sallée, E. Shuckburgh, N. Bruneau, A. J. S. Meijers, T. J. Bracegirdle, and Z. Wang. Assessment of southern ocean mixed-layer depths in CMIP5 models: Historical bias and forcing response. *J. Geophys. Res. Oceans*, 118(4):1845–1862, apr 2013a. doi: 10.1002/jgrc.20157. URL <http://dx.doi.org/10.1002/jgrc.20157>.

- J.-B. Sallée, E. Shuckburgh, N. Bruneau, A. J. S. Meijers, T. J. Bracegirdle, Z. Wang, and T. Roy. Assessment of southern ocean water mass circulation and characteristics in cmip5 models: Historical bias and forcing response. *Journal of Geophysical Research: Oceans*, 118(4):1830–1844, 2013b. ISSN 2169-9291. doi: 10.1002/jgrc.20135. URL <http://dx.doi.org/10.1002/jgrc.20135>.
- J. L. Sarmiento and N. Gruber. *Ocean Biogeochemical Dynamics*. Princeton University Press, 2006.
- K. D. Six and E. Maier-Reimer. Effects of plankton dynamics on seasonal carbon fluxes in an ocean general circulation model. *Global Biogeochemical Cycles*, 10(4):559–583, 1996. ISSN 1944-9224. doi: 10.1029/96GB02561. URL <http://dx.doi.org/10.1029/96GB02561>.
- E. L. Smith. Photosynthesis in relation to light and carbon dioxide. *Proc. Nat. Acad. Sci.*, 22:504–511, 1936.
- K. Speer, S. R. Rintoul, and B. Sloyan. The diabatic deacon cell. *Journal of Physical Oceanography*, 30(12):3212–3222, 2000. doi: 10.1175/1520-0485(2000)030<3212:TDDC>2.0.CO;2. URL [http://dx.doi.org/10.1175/1520-0485\(2000\)030<3212:TDDC>2.0.CO;2](http://dx.doi.org/10.1175/1520-0485(2000)030<3212:TDDC>2.0.CO;2).
- B. Stevens, M. Giorgetta, M. Esch, T. Mauritsen, T. Crueger, S. Rast, M. Salzmann, H. Schmidt, J. Bader, K. Block, R. Brokopf, I. Fast, S. Kinne, L. Kornblueh, U. Lohmann, R. Pincus, T. Reichler, and E. Roeckner. Atmospheric component of the MPI-M Earth System Model: ECHAM6. *Journal of Advances in Modeling Earth Systems*, 5(2):146–172, 2013. ISSN 1942-2466. doi: 10.1002/jame.20015. URL <http://dx.doi.org/10.1002/jame.20015>.
- A. Stössel, D. Notz, F. A. Haumann, H. Haak, J. Jungclaus, and U. Mikolajewicz. Controlling high-latitude southern ocean convection in climate models. *Ocean Modelling*, 86: 58 – 75, 2015. ISSN 1463-5003. doi: <http://dx.doi.org/10.1016/j.ocemod.2014.11.008>. URL <http://www.sciencedirect.com/science/article/pii/S1463500314001760>.
- H. U. Sverdrup. On conditions for the vernal blooming of phytoplankton. *Journal du Conseil International pour l'Exploration de la Mer*, 18:287–295, 1953.

- A. Tagliabue, J.-B. Sallée, A. R. Bowie, M. Lévy, S. Swart, and P. W. Boyd. Surface-water iron supplies in the southern ocean sustained by deep winter mixing. *Nature Geoscience*, 7(4):314–320, mar 2014. doi: 10.1038/ngeo2101. URL <https://doi.org/10.1038%2Fngeo2101>.
- T. Takahashi, J. Olafsson, J. Goddard, D. W. Chipman, and S. C. Sutherland. Seasonal variation of co₂ and nutrients in the high-latitude surface oceans: a comparative study. *Global Biogeochem. Cycles*, 7:843–878, 1993.
- T. Takahashi, S. C. Sutherland, C. Sweeney, A. Poisson, N. Metzl, B. Tilbrook, N. Bates, R. Wanninkhof, R. A. Feely, C. Sabine, J. Olafsson, and Y. Nojiri. Global seaair co₂ ux based on climatological surface ocean and pco and seasonal biological and temperature effects. *Deep-Sea Research II*, 2002.
- L. D. Talley. Closure of the global overturning circulation through the indian, pacific and southern oceans: schematics and transports. *Oceanography*, 26(1):80–97, 2013. URL http://pordlabs.ucsd.edu/ltalley/papers/2010s/talley_GOC_oceanography_feb2013.pdf.
- J. Taucher and A. Oschlies. Can we predict the dirdirect of marine primary production change under global warming? *Geophys. Res. Lett.*, 38, 2011. doi: 10.1029/2010GL045934.
- K. E. Taylor, R. J. Stouffer, and G. A. Meehl. An overview of CMIP5 and the experiment design. *Bull. Amer. Meteor. Soc.*, 93(4):485–498, apr 2012. doi: 10.1175/bams-d-11-00094.1. URL <http://dx.doi.org/10.1175/BAMS-D-11-00094.1>.
- D. Thompson and J. Wallace. Annular modes in the extratropical circulation. part i: Month-month variability. *Journal of Climate*, 13(5):1000–1016, 2000. doi: 10.1175/1520-0442(2000)013<1000:AMITEC>2.0.CO;2. URL <http://journals.ametsoc.org/doi/pdf/10.1175/1520-0442%282000%29013%3C1040%3AR%3E2.0.CO%3B2>.
- D. W. J. Thompson, S. Solomon, P. J. Kushner, M. H. England, K. M. Grise, and D. J. Karoly. Signatures of the antarctic ozone hole in southern hemisphere surface climate change. *Nature Geoscience*, 4(11):741–749, oct 2011. doi: 10.1038/ngeo1296. URL <http://dx.doi.org/10.1038/NGE01296>.

- D. W. J. Thompson, E. A. Barnes, C. Deser, W. E. Foust, and A. S. Phillips. Quantifying the role of internal climate variability in future climate trends. *Journal of Climate*, 28(16):6443–6456, aug 2015. doi: 10.1175/jcli-d-14-00830.1. URL <http://dx.doi.org/10.1175/JCLI-D-14-00830.1>.
- T. Volk and M. I. Hoffert. *Ocean Carbon Pumps: Analysis of Relative Strengths and Efficiencies in Ocean-Driven Atmospheric CO₂ Changes*, pages 99–110. American Geophysical Union, 1985. ISBN 9781118664322. doi: 10.1029/GM032p0099. URL <http://dx.doi.org/10.1029/GM032p0099>.
- L. Wang, J. Huang, Y. Luo, and Z. Zhao. Narrowing the spread in CMIP5 model projections of air-sea CO₂ fluxes. *Scientific Reports*, 6:37548, nov 2016. doi: 10.1038/srep37548. URL <https://doi.org/10.1038%2Fsrep37548>.
- S. Wang and J. K. Moore. Variability of primary production and air-sea CO₂ flux in the Southern Ocean. *Global Biogeochemical Cycles*, 26(1):n/an/a, 2012. ISSN 1944-9224. doi: 10.1029/2010GB003981. URL <http://dx.doi.org/10.1029/2010GB003981>. GB1008.
- R. Wanninkhof. Relationship between wind speed and gas exchange over the ocean. *Journal of Geophysical Research: Oceans*, 97(C5):7373–7382, 1992. ISSN 2156-2202. doi: 10.1029/92JC00188. URL <http://dx.doi.org/10.1029/92JC00188>.
- R. Weiss. Carbon dioxide in water and seawater: the solubility of a non-ideal gas. *Marine Chemistry* 2, 2:203–215, 1974. doi: doi:10.1016/0304-4203(74)90015-2. URL <http://www.sciencedirect.com/science/article/pii/0304420374900152>.
- X. Yuan. ENSO-related impacts on antarctic sea ice: a synthesis of phenomenon and mechanisms. *Antarctic Science*, 16(4):415–425, dec 2004. doi: 10.1017/s0954102004002238. URL <https://doi.org/10.1017%2Fs0954102004002238>.

List of Figures

1	Schematic overview on the different components in MPI-Earth-System-Model with a non-interactive carbon cycle [Giorgetta et al., 2013]	5
2	Schematic overview of the global ocean biogeochemistry model HAMOCC [Ilyina et al., 2013] which is coupled to the atmospheric model component ECHAM and the ocean model MPIOM. The ocean model provides state variables of physical oceanography, i.e. ice cover, temperature (T), salinity (S) and the advective velocities (\bar{v}). The water column holds tracers of gases, i.e. oxygen (O_2), nitrogen (N_2), laughing gas (N_2O), and dimethyl sulfide (DMS); nutrients, i.e. iron (Fe), phosphate (PO_4), nitrate (NO_3) and silicic acid $Si(OH)_4$; and tracers of carbonate chemistry, i.e. dissolved inorganic carbon (TCO_2) and total alkalinity (TA). Photosynthesis converts DIC and nutrients to organic carbon, which produces calcium carbon ($CaCO_3$) or opal shells.	8
3	Spatial distribution of the climatology (a,c) and decadal internal variability σ_{DIV} (b,d) from 1980-2004 of the Southern Ocean air-sea CO_2 flux: MPI-ESM LE ensemble mean as forced signal (a), ensemble decadal standard deviation as decadal internal variability σ_{DIV} (b), SOM-FFN climatology 1982-2004 (c), SOM-FFN decadal variability σ_{DIV} (d); negative values indicate ocean uptake.	16
4	Temporal evolution of the Southern Ocean air-sea CO_2 flux south of 35°S. Grey lines show the 100 ensemble members, the black line the ensemble mean, the blue shading is the ensemble decadal internal variability σ_{DIV} , the red line shows a positive CO_2 flux trend, the blue line shows a negative CO_2 flux trend, the green line represents the SOM-FFN observation-based estimate [Landschützer et al., 2015]; negative values indicate carbon uptake	17
5	Spatial distribution of the Southern Ocean sea-level pressure and wind vectors overlain as arrows: ensemble mean climatology from 1980 to 2004 (a) as forced signal and ensemble decadal standard deviation (b) as decadal internal variability σ_{DIV} ; and the difference between MPI-ESM and reanalysis data from NCEP climatology [Kalnay et al., 1996] (c), and decadal internal variability σ_{DIV} from NCEP climatology (d).	20

6	Temporal evolution of the annual Southern Annular Mode (SAM) index according to [Gong and Wang, 1999]. Grey lines show the 100 ensemble members; the black line the ensemble mean; the blue shading is the decadal internal variability σ_{DIV} ; the red line represents positive CO ₂ flux trend; the blue line shows the negative CO ₂ flux trend; the green line shows the station-based SAM from Marshall [2003]	21
7	Spatial distribution of the vertically integrated primary production in the Southern Ocean: climatological ensemble mean from 1980 to 2004 (left) as forced signal and ensemble decadal anomaly standard deviation (right) as decadal internal variability σ_{DIV}	23
8	Spatial distribution of the climatology of surface nitrate (left) compared with WOA data [Garcia et al., 2013] (right)	23
9	Temporal evolution of the vertically integrated primary production in the Southern Ocean south of 35°S. Grey lines show the 100 ensemble members, the black line the ensemble mean, the blue shading is the decadal internal variability σ_{DIV} , the red line represents the positive CO ₂ flux trend, the blue line represents negative CO ₂ flux trend	25
10	Zonally averaged transect of the Southern Ocean and the upper-ocean overturning circulation; black arrows show yearly mean advective transports of water in Sv (a) and carbon in PgC/yr (b) and its decadal internal variability σ_{DIV} ; white lines are isopyncals separating Sub-Antarctic Mode Water (SAMW) at potential density $\rho_\theta = 1026.5 \text{ kg m}^{-3}$ from Antarctic Intermediate Water (AAIW), at $\rho_\theta = 1027.2 \text{ kg m}^{-3}$ from Circumpolar Deep Water (CDW), at $\rho_\theta = 1027.7 \text{ kg m}^{-3}$ from Antarctic Bottom Water (AABW); the black line is the mixed-layer depth (MLD); the colored contours show the distribution of dissolved inorganic carbon (DIC)	27
11	Spatial distribution of the ensemble mean climatology (1980-2004) of the mixed-layer depth (MLD) (left) compared with Monterey & Levitus, 1997 NOAA Atlas	28

12	Linear trends in the Southern Annular Mode (SAM) as indicator of wind strength vs. CO ₂ flux at 50-60°S; each data point represents 8-year trends of a single realization normalized for the ensemble mean trend between 1980 and 2005; the blue dot is the most negative monotonic CO ₂ flux trend; the red dot is positive monotonic CO ₂ flux trend.	30
13	Linear trends in ΔpCO ₂ (left) and sea-level pressure and wind vectors overlain as arrows (right) for the case of the most positive monotonic 8-year CO ₂ flux trend; hatched areas indicate where trends are outside the 5% significance level	31
14	Linear trends in pCO _{2,thermal} (left) and ΔpCO _{2,non-thermal} (right) for the case of the most positive monotonic 8-year CO ₂ flux trend; hatched areas indicate where trends are outside the 5% significance level	32
15	Linear trends in Ekman transport and Ekman pumping in the case of the most positive 8-years CO ₂ flux trend; hatched areas indicate where trends are outside the 5% significance level	33
16	Zonally averaged upper-ocean overturning circulation in the case of the most positive 8-year CO ₂ flux trend; black arrows show mean advective carbon transport, red arrows show positive advective carbon transport trends; blue arrows show negative advective carbon transport trends; black numbers quantify the trends in advective carbon transport in PgC/8yrs; white lines are isopycnals as in fig. 10; grey line is mixed-layer depth (MLD) in the beginning and the black line MLD in the end of the period.	34
17	Southern Ocean austral summer trends for the case of the most positive 8-year CO ₂ flux trend: CO ₂ flux (a), vertically integrated primary production (b), nutrient availability factor (c), surface temperature & limitation function (d), mixed layer depth (e); average depth of vertical diffusivity due to wind (f) and phytoplankton average depth (g); hatched areas indicate where trends are outside the 5% significance level	37
18	Linear trends in ΔpCO ₂ (left) and sea-level pressure and wind vectors overlain as arrows (right) for the case of the most negative monotonic 8-year CO ₂ flux trend; hatched areas indicate where trends are outside the 5% significance level	38

19	Linear trends in $p\text{CO}_{2,\text{thermal}}$ (left) and $\Delta p\text{CO}_{2,\text{non-thermal}}$ (right) for the case of the most negative monotonic 8-year CO_2 flux trend; hatched areas indicate where trends are outside the 5% significance level	39
20	Linear trends in Ekman transport and Ekman pumping in the case of the most negative 8-years CO_2 flux trend; hatched areas indicate where trends are outside the 5% significance level	40
21	Zonally averaged upper-ocean overturning circulation in the case of the most negative 8-year CO_2 flux trend; black arrows show mean advective carbon transport, red arrows show positive advective carbon transport trends; blue arrows show negative advective carbon transport trends; black numbers show the trends in advective carbon transport in $\text{PgC}/8\text{yrs}$; white lines are isopyncals as in fig. 10; grey line is mixed-layer depth (MLD) in the beginning and the black line MLD in the end of the period.	41
22	Southern Ocean austral summer trends for the most negative 8-year CO_2 flux trend: CO_2 flux (a), vertically integrated primary production (b), nutrient availability factor (c), surface temperature & limitation function (d), mixed layer depth (e); average depth of vertical diffusivity due to wind (f) and phytoplankton average depth (g); hatched areas indicate where trends are outside the 5% significance level	43
23	Schematic illustration of $p\text{CO}_2$ driver separation assuming a well-mixed zonal carbon box of the upper-ocean, where CO_2 flux (red) is separated in contributions due to thermal (orange), freshwater (light blue), biology (green) and a residual for circulation (dark blue)	44

24	Schematic illustration of the Southern Ocean under the context of increasing westerly winds and response in the thermal effect, biology and upper-ocean circulation leading towards a positive CO ₂ flux trend; red color-coding indicates a relative increase of the related quantity or process whereas blue indicates a relative decrease. Stronger winds enhance the upper-ocean overturning circulation. Increased upwelling increases outgassing of over-saturated carbon-rich deep waters. Increased Ekman transport advects DIC further north, cools the higher latitudes whereas it warms the lower latitudes. Deeper mixing and cooling in the higher latitudes decreases primary production whereas shallower mixing and warming increase primary production in the higher latitudes.	48
25	Schematic illustration of the Southern Ocean under the context of decreasing westerly winds and response in the thermal effect, biology and upper-ocean circulation leading towards a negative CO ₂ flux trend; red color-coding indicates a relative increase of the related quantity or process, whereas blue indicates a relative decrease. Stronger winds decrease the upper-ocean overturning circulation. Decreased upwelling lowers outgassing of over-saturated carbon-rich deep waters. Decreased Ekman transport advects less DIC to the north, warms the higher latitudes whereas it cools the lower latitudes. Shallower mixing and warming in the higher latitudes increases primary production, whereas deeper mixing and cooling decrease primary production in the higher latitudes.	50
A.1	Southern Ocean carbon sink: yearmean fieldsum 35-90S (left) and yearmean in a random grid cell (right)	72
A.2	Southern Ocean carbon sink trends per trendlength	74
A.3	Southern Ocean carbon sink trends per trendlength; corrected for forced trend	75
A.4	Spatial distribution of the climatology of surface DIC (left) compared with GLODAPv2 data [Garcia et al., 2013] (right)	76
A.5	Spatial distribution of the climatological ensemble mean surface phosphate from 1980 to 2004 (left) compared with World Ocean Atlas (WOA) climatological data [Garcia et al., 2013] (right)	76

A.6 Spatial distribution of the ensemble mean climatology (1980-2004) of the sea-surface temperature (SST) (left) compared with WOCE climatology	77
A.7 Linear austral summer trends in sea-surface temperature (SST) for the case of the most positive monotonic 8-year CO ₂ flux trend; hatched areas indicate where trends are outside the 5% significance level	78
A.8 Linear austral summer trends in sea-surface temperature (SST) for the case of the most negative monotonic 8-year CO ₂ flux trend; hatched areas indicate where trends are outside the 5% significance level	78
A.9 Linear summer trends for the case of the most positive monotonic 8-year CO ₂ flux trend; ΔpCO ₂ (a) and sea-level pressure & winds (b); pCO _{2,thermal} (c) and ΔpCO _{2,non-thermal} (d); hatched areas indicate where trends are outside the 5% significance level	79
A.10 Linear winter trends for the case of the most positive monotonic 8-year CO ₂ flux trend; ΔpCO ₂ (a) and sea-level pressure & wind vectors overlain as arrows (b); pCO _{2,thermal} (c) and ΔpCO _{2,non-thermal} (d); hatched areas indicate where trends are outside the 5% significance level	80
A.11 Linear summer trends for the case of the most negative monotonic 8-year CO ₂ flux trend; ΔpCO ₂ (a) and sea-level pressure & wind vectors overlain as arrows (b); pCO _{2,thermal} (c) and ΔpCO _{2,non-thermal} (d); hatched areas indicate where trends are outside the 5% significance level	81
A.12 Linear winter trends for the case of the most negative monotonic 8-year CO ₂ flux trend; ΔpCO ₂ (a) and sea-level pressure & wind vectors overlain as arrows (b); pCO _{2,thermal} (c) and ΔpCO _{2,non-thermal} (d); hatched areas indicate where trends are outside the 5% significance level	82
A.13 Combined light- & temperature limitation function for the average phytoplankton growth rate in HAMOCC	83

A Supplementary information

A.1 Statistics of Southern Ocean carbon sink

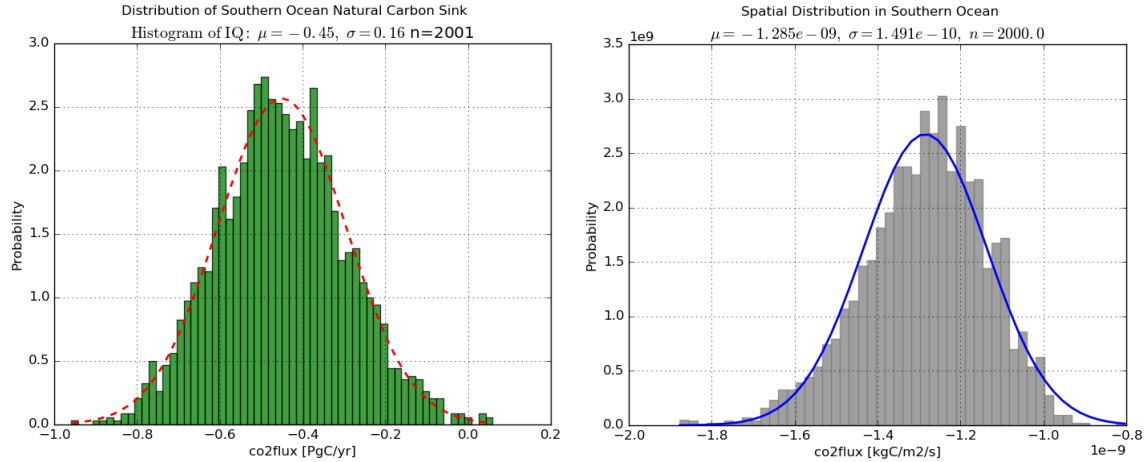


Figure A.1: Southern Ocean carbon sink: yearmean fieldsum 35-90S (left) and yearmean in a random grid cell (right)

A.2 CO₂ flux trends

CO₂flux trends heatmap in MPI-ESM Large Ensemble

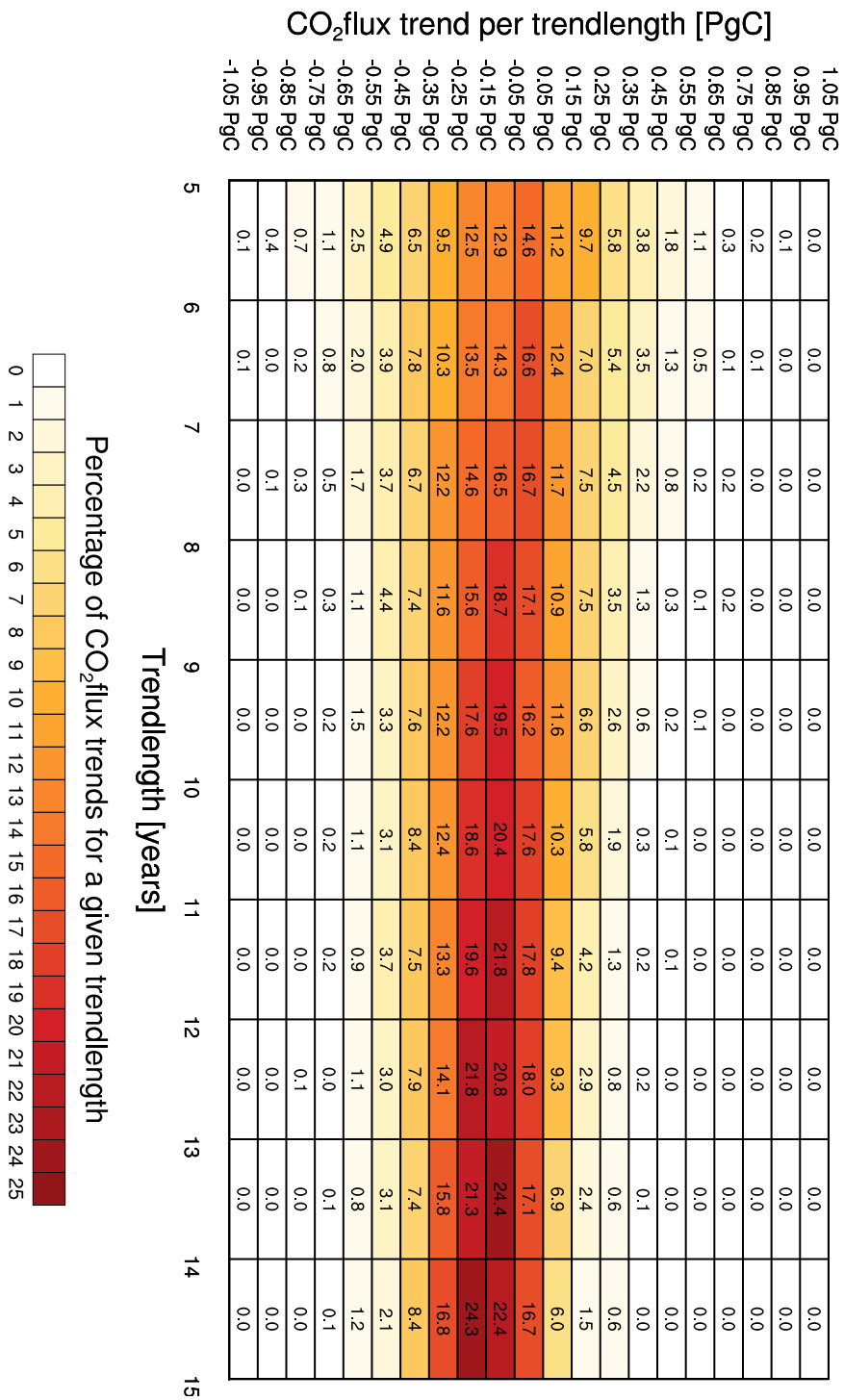


Figure A.2: Southern Ocean carbon sink trends per trendlength

CO₂flux trends heatmap in MPI-ESM Large Ensemble

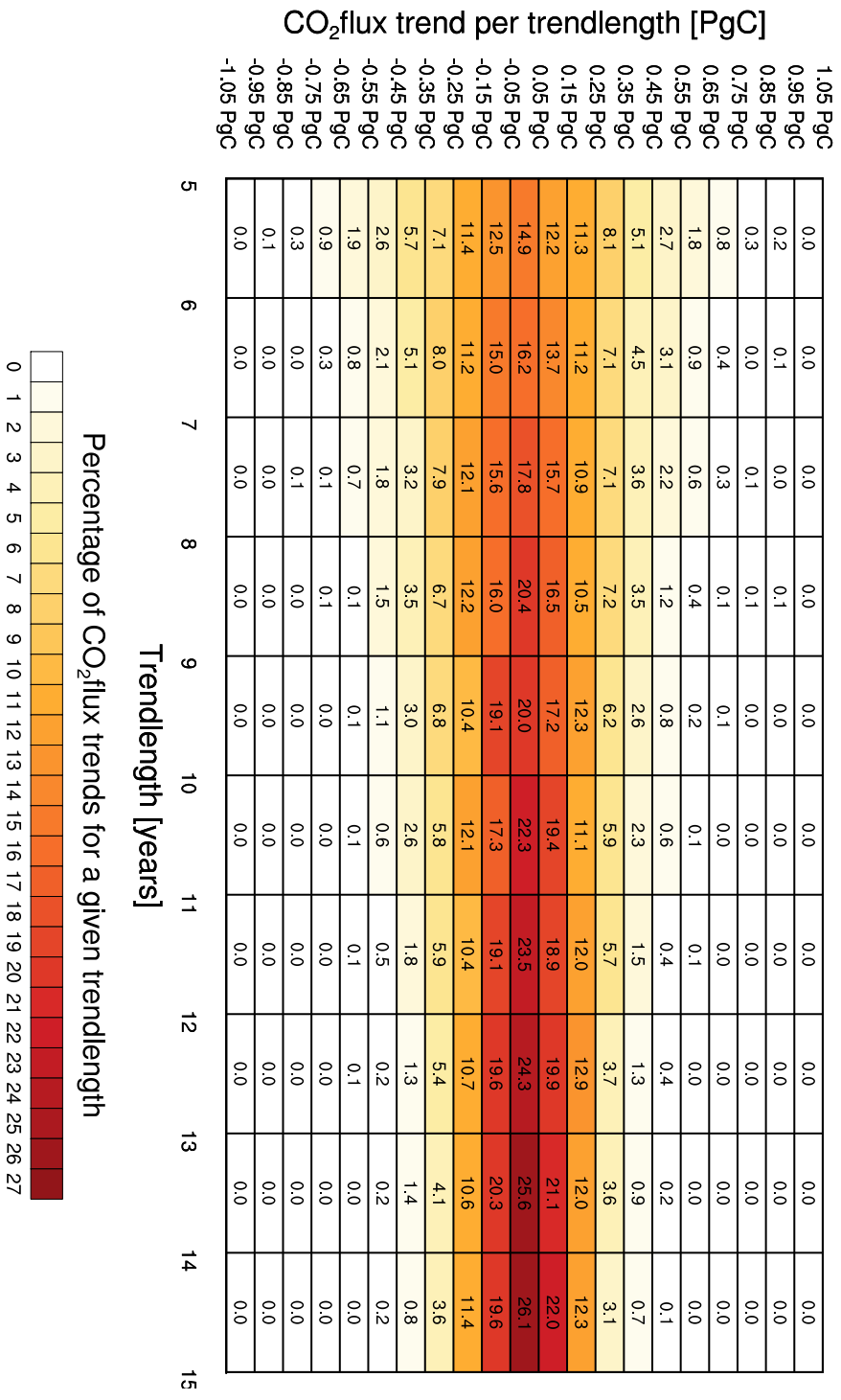


Figure A.3: Southern Ocean carbon sink trends per trendlength; corrected for forced trend

A.3 Model evaluation additum

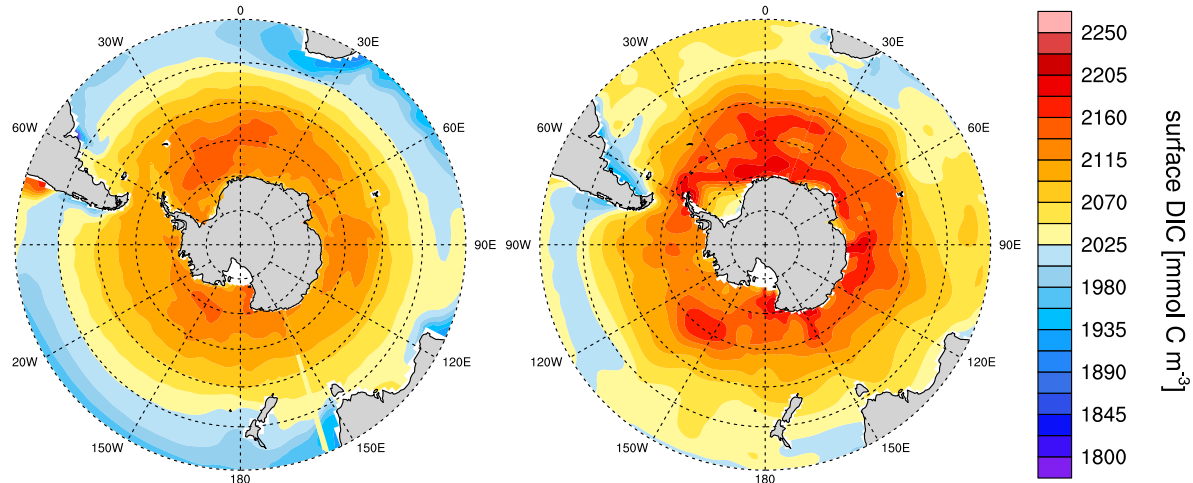


Figure A.4: Spatial distribution of the climatology of surface DIC (left) compared with GLODAPv2 data [Garcia et al., 2013] (right)

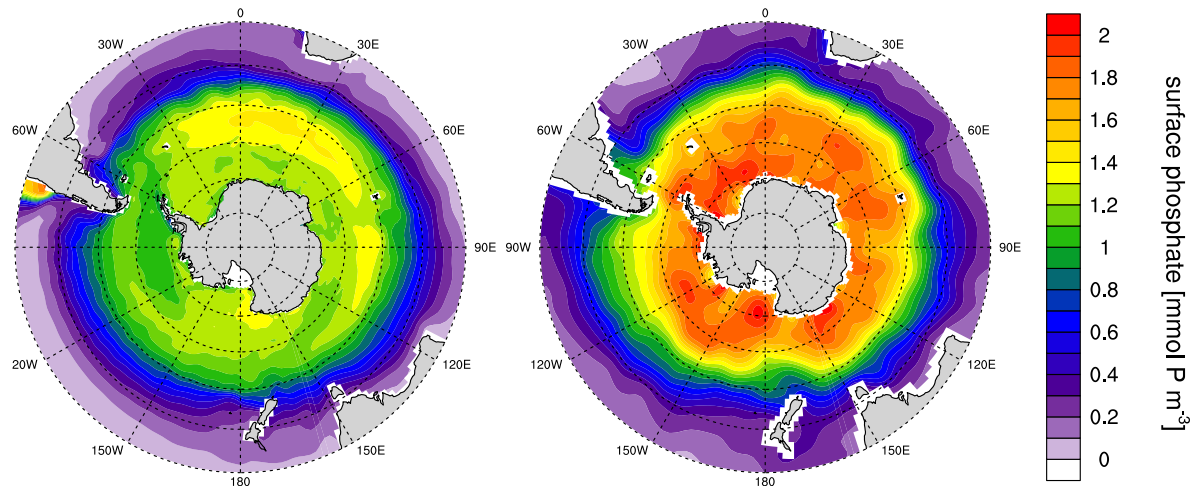


Figure A.5: Spatial distribution of the climatological ensemble mean surface phosphate from 1980 to 2004 (left) compared with World Ocean Atlas (WOA) climatological data [Garcia et al., 2013] (right)

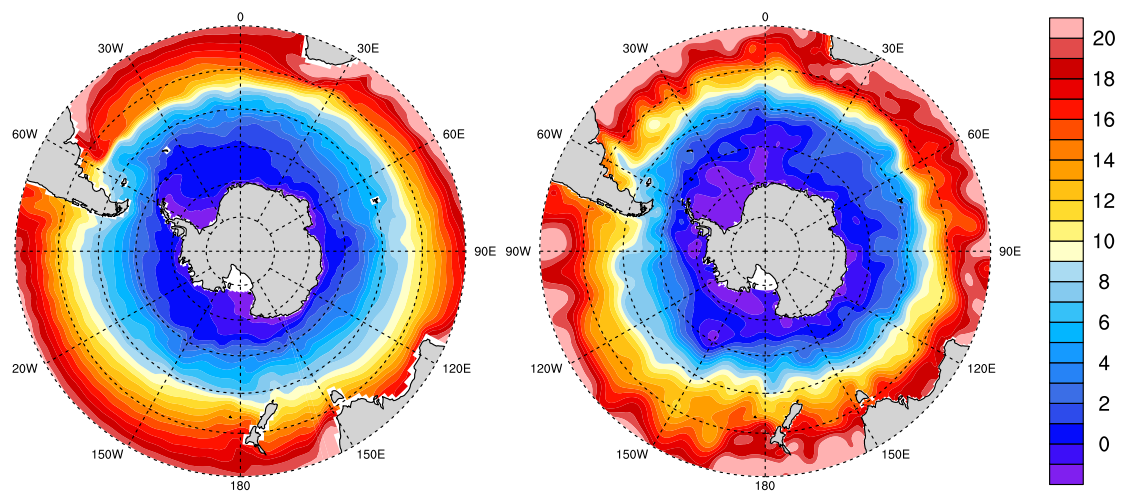


Figure A.6: Spatial distribution of the ensemble mean climatology (1980-2004) of the sea-surface temperature (SST) (left) compared with WOCE climatology

A.4 Trends Additum

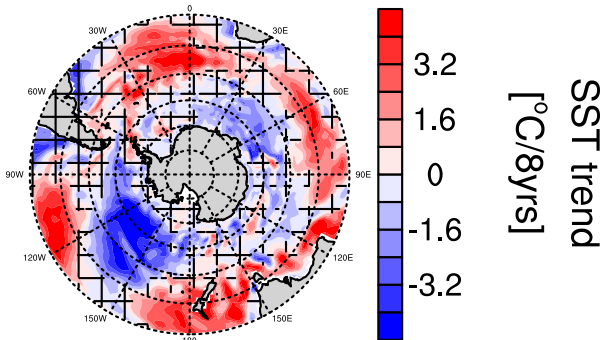


Figure A.7: Linear austral summer trends in sea-surface temperature (SST) for the case of the most positive monotonic 8-year CO₂ flux trend; hatched areas indicate where trends are outside the 5% significance level

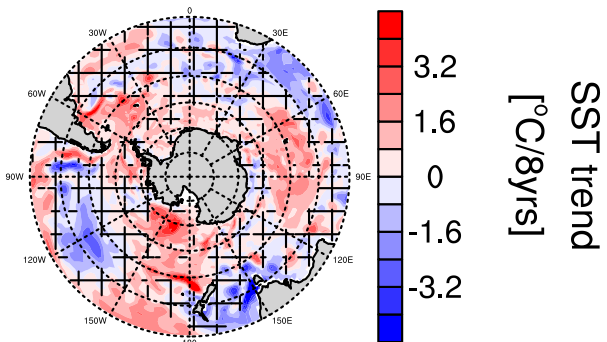


Figure A.8: Linear austral summer trends in sea-surface temperature (SST) for the case of the most negative monotonic 8-year CO₂ flux trend; hatched areas indicate where trends are outside the 5% significance level

A.5 Thermal separation by seasons

A.6 Positive CO₂ flux trend

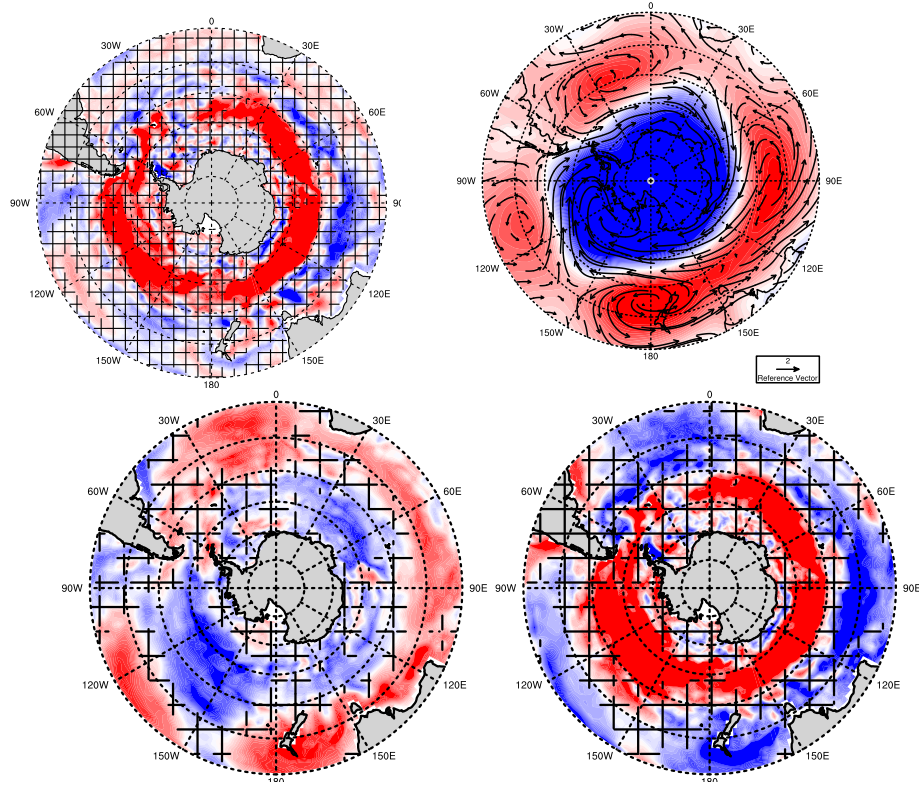


Figure A.9: Linear summer trends for the case of the most positive monotonic 8-year CO₂ flux trend; $\Delta p\text{CO}_2$ (a) and sea-level pressure & winds (b); $p\text{CO}_{2,\text{thermal}}$ (c) and $\Delta p\text{CO}_{2,\text{non-thermal}}$ (d); hatched areas indicate where trends are outside the 5% significance level

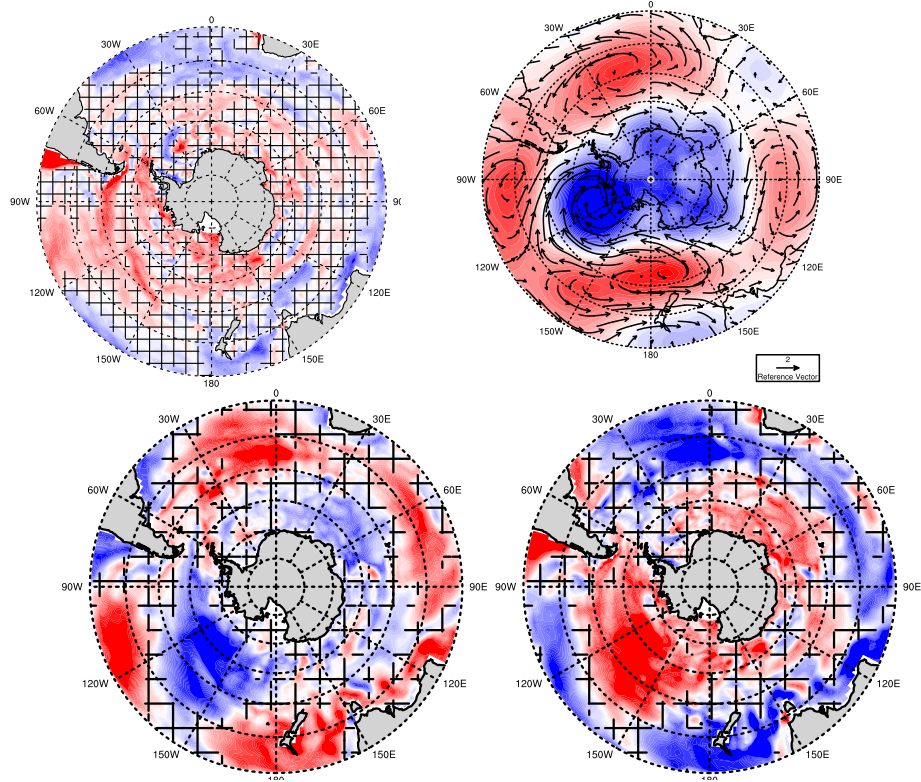


Figure A.10: Linear winter trends for the case of the most positive monotonic 8-year CO₂ flux trend; $\Delta p\text{CO}_2$ (a) and sea-level pressure & wind vectors overlain as arrows (b); pCO_{2,thermal} (c) and $\Delta p\text{CO}_{2,\text{non-thermal}}$ (d); hatched areas indicate where trends are outside the 5% significance level

A.7 Negative CO₂ flux trend

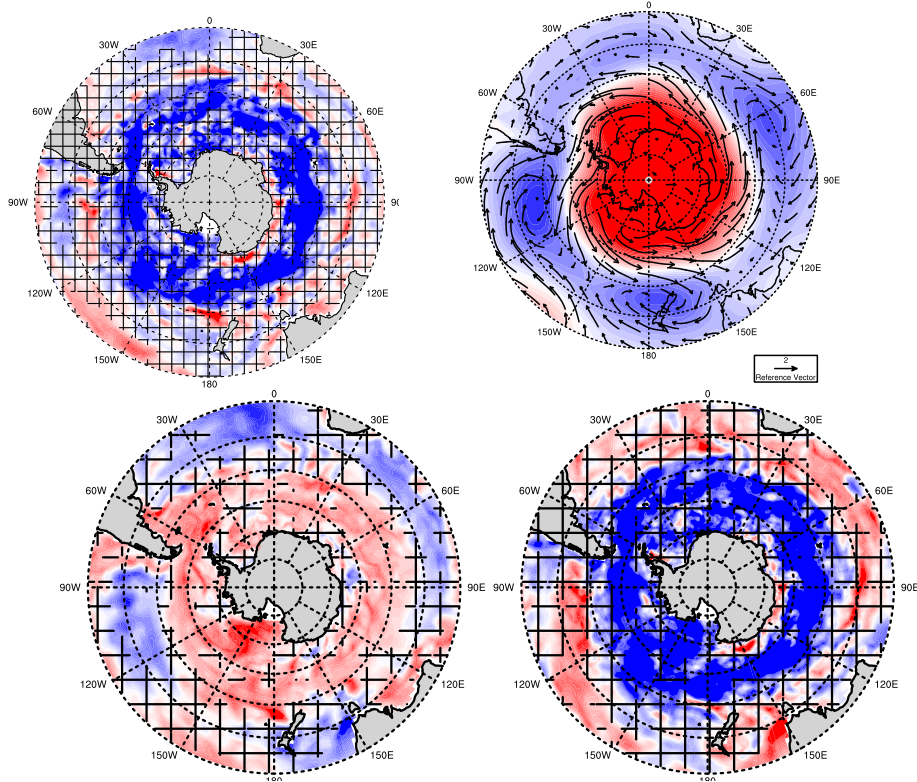


Figure A.11: Linear summer trends for the case of the most negative monotonic 8-year CO₂ flux trend; $\Delta p\text{CO}_2$ (a) and sea-level pressure & wind vectors overlaid as arrows (b); $p\text{CO}_2\text{,thermal}$ (c) and $\Delta p\text{CO}_2\text{,non-thermal}$ (d); hatched areas indicate where trends are outside the 5% significance level

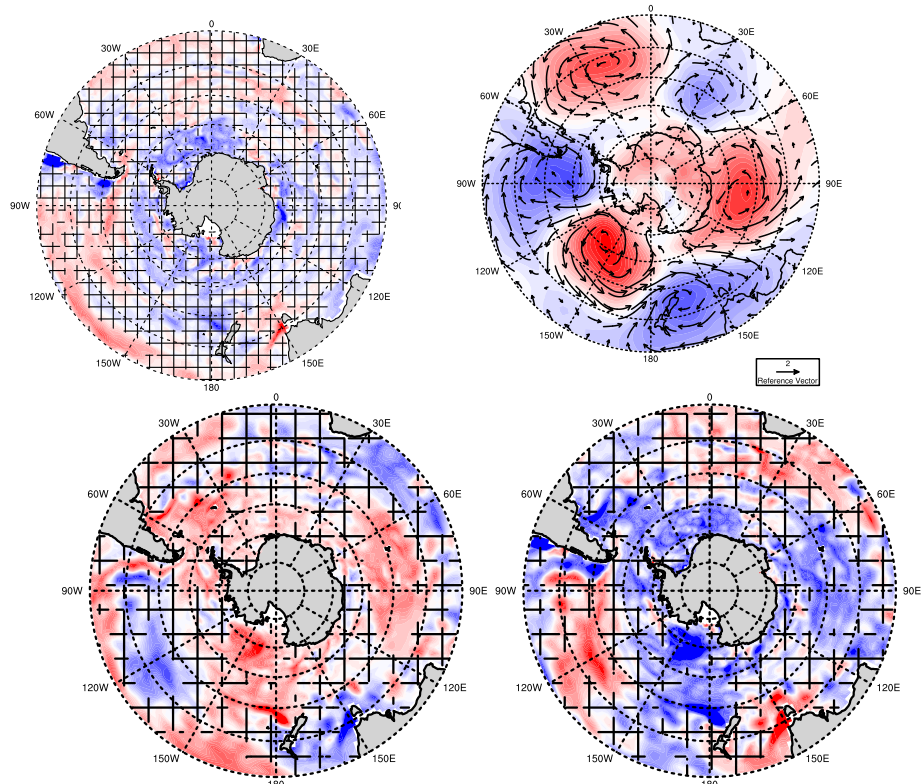


Figure A.12: Linear winter trends for the case of the most negative monotonic 8-year CO_2 flux trend; $\Delta p\text{CO}_2$ (a) and sea-level pressure & wind vectors overlaid as arrows (b); $p\text{CO}_{2,\text{thermal}}$ (c) and $\Delta p\text{CO}_{2,\text{non-thermal}}$ (d); hatched areas indicate where trends are outside the 5% significance level

A.8 Misc

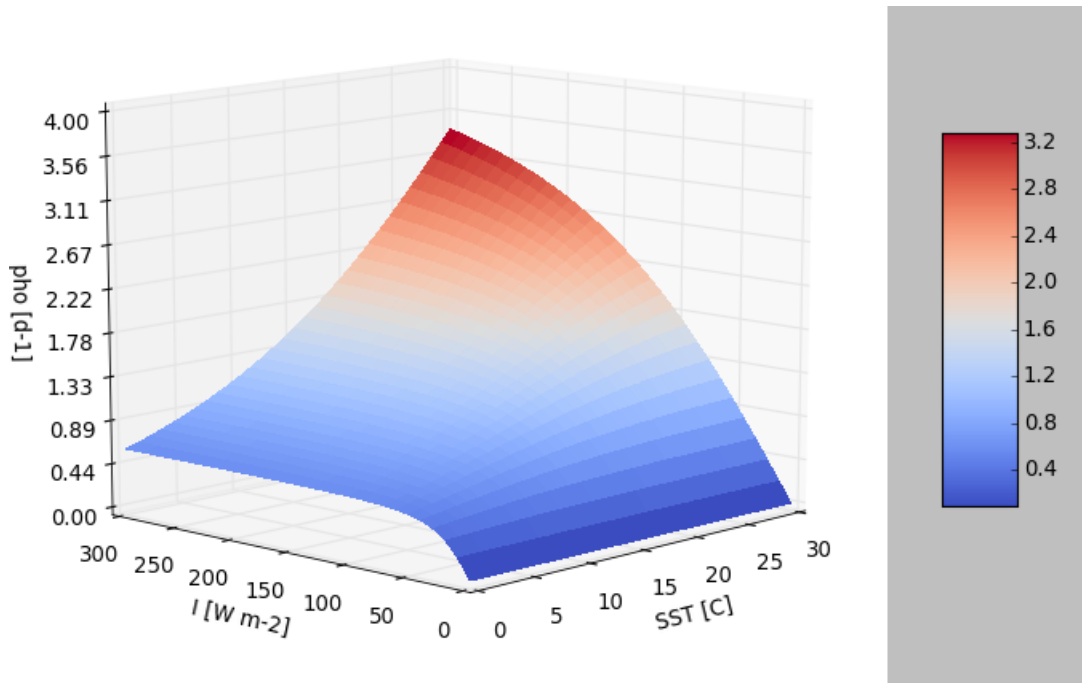


Figure A.13: Combined light- & temperature limitation function for the average phytoplankton growth rate in HAMOCC